

Condensed phase spectroscopy from mixed-order semiclassical molecular dynamics: Absorption, emission, and resonant Raman spectra of I₂ isolated in solid Kr

M. Ovchinnikov and V. A. Apkarian

Department of Chemistry, University of California, Irvine, California 92697-2025

(Received 5 August 1996; accepted 10 September 1996)

A method for spectral simulations in systems of very large dimensionality via semiclassical molecular dynamics is introduced and applied to the spectroscopy of iodine isolated in solid Kr, as a prototype of spectroscopy in condensed media in general. The method relies on constructing quantum correlation functions, $C(t)$, using initial value propagators which correspond to the zeroth- and second-order approximations in stationary phase of the exact quantum propagator. The first is used for treating modes with high thermal occupation numbers, the lattice modes, while the second is used for treating the guest mode. The limits of validity of the bare propagators are tested vs exact treatments of gas phase I₂, and shown to be quite broad. The mixed order simulations are then used to reproduce the structured $A \rightarrow X$ emission, the structureless $B \leftarrow X$ absorption, and the intensities in resonant Raman (RR) progressions of matrix isolated I₂, connecting spectroscopic observables to molecular motions. Decompositions of the supersystem correlations into system and bath are used to provide perspectives about condensed phase spectroscopy. The system correlation can be regarded as the sampling function for the decaying bath correlation, which in turn is a summary of the many-body dynamics. The $B \leftarrow X$ absorption spectrum is determined by the coherent ballistic motion of the excited state density: Upon stretching, I₂ pushes the cage atoms out of overlap in position density, and $C(t)$ never recovers. Due to the compressive nature of the cage coordinate in the $A \rightarrow X$ transition, $C(t)$ decays more gently, after being sampled three times. RR spectra, which are reproduced with adiabatic dynamics, sample the complete history of the many-body correlations, however, due to the breadth in space-time of scattering into high overtones, the sampling is coarse grained. The specific dynamics that control $C(t)$ cannot be described as dissipative. © 1996 American Institute of Physics. [S0021-9606(96)00647-2]

I. INTRODUCTION

That spectroscopy in condensed media is most naturally treated in terms of quantum correlation functions, has been well entrenched in the literature on condensed matter physics.^{1,2} The seminal review article by Gordon has perhaps been the most influential in introducing the framework to systems of chemical interest,³ and in sowing the seeds of time-dependent treatments of gas phase spectroscopy, the “semiclassical way to spectroscopy” of systems of low dimensionality, spearheaded by Heller and co-workers.^{4,5} Exact evaluation of quantum correlation functions in condensed media is not feasible, since the time-development of a quantum Hamiltonian of large dimensionality is not possible. To proceed, a system–bath separation is made, in which the reduced dimensionality of the system affords a more rigorous treatment of its dynamics, while the bath representing all other degrees of freedom is treated through abstractions useful for various phenomenology. Where the conditions of a weak coupling between system and bath prevail, correlation functions can be pieced together as ensemble averaged interactions at short time and linear dissipation at longer times through the well refined tools of quantum dissipative processes.⁶ By construct, the information content of such treatments remains limited to characterization of line shapes in terms of static (inhomogeneous) and dynamical (homo-

neous) contributions. The artificial distinction between these two contributions, which differ by their fluctuation time scales, can be eliminated in stochastic models that smoothly bridge the two limits.^{7–9} Such treatments have been extended to nonlinear spectroscopies, to Raman and beyond,¹⁰ through multiple time correlation functions, as systematically developed in the monograph by Mukamel.¹¹ Such Brownian oscillator models have been implemented in simulations that lend themselves to microscopic interpretations, as exemplified in the recent treatment of fluorescence,¹² resonant Raman,¹³ and impulsive stimulated Raman¹⁴ spectra of I₃[−] in liquids. Moreover, the model is useful in codifying real-time observables in ultrafast spectroscopies, of which third-order nonlinear spectroscopies represent the more important class, as recently outlined in a rather comprehensive review.¹⁵ The formalism also connects time-resolved nonlinear spectroscopies to solvent spectral densities,¹⁶ which in turn may be extracted from molecular dynamics simulations, or from instantaneous normal mode analyses.¹⁷ In short, within the framework of linear response theories, spectral observables in condensed media can be related to quantum correlation functions of a system coupled to a bath, and then indirectly related to molecular motions and forces.

Three fundamental aspects are less than satisfactory in the present state of treatments of condensed phase spectroscopy, as described above. These are: (a) the requisite but

artificial distinction between system and bath; (b) the indirect connection between observables and the underlying molecular mechanics, (c) the necessary assumption of linear response in making such connections. The latter approximation obviously hinges upon the assumption of small perturbations, which is not easily justified in the case of electronic transitions. Consider, for example, the dissociative excitation of a solute molecule in condensed phase. The early time evolution of the system, which is solely responsible for the frequency domain spectra, now might be dominated by highly nonlinear and specific molecular motions—processes that cannot be contained in a language limited to dissipation or averaged dynamics, and may not even be related to spectral densities obtained from equilibrium configurations of the solvent. Classical mechanics provides a more natural language for describing such nonlinear phenomena. The nearly quantitative reproduction of time domain spectral observables in recent pump–probe studies of photodissociation/recombination,¹⁸ vibrational relaxation, and electronic predissociation,¹⁹ in cryogenic matrices, serve as our inspiration that a similar approach may be feasible in treating frequency domain spectra. While the core of such treatments relies on solving coupled classical equations of motion for hundreds of particles, in simulating experimental observables, quantum considerations are incorporated implicitly through initial conditions and by taking appropriate ensemble averages.^{18–22} It is, for example, possible to account for the coherence of the radiation fields (chirp) used in the preparation and interrogation of nonstationary states in such classical simulations.²² Quite clearly, the molecular motions that shape the time domain observables must also determine the frequency domain spectra. Then, to the extent that the nuclear motions can be represented by classical dynamics, it should be possible to simulate spectra and to interpret their features in terms of properly “dressed” molecular dynamics from which quantum many-body correlation functions may be constructed. In this paper we present such a treatment. The core of the approach relies on molecular dynamics, where no separation between system and bath is required, and no assumption about linearity of dynamics is necessary. The formulation uses semiclassical propagators in constructing many-body correlations, and is closely related to methods advanced recently in treatments of gas phase spectroscopy,^{23–27} and has already been suggested by Cao and Voth as a possible means for describing quantum time correlation functions in condensed media.²⁸ We will specialize to the analysis of the spectroscopy of I₂ isolated in rare gas matrices, complementing the prior time domain studies of the same, and enabling comparisons with both experiments and other theoretical treatments of this prototype. We should point out at the outset that this is a prototype of condensed phase systems in general, not limited to matrices. On the time scales of relevance, the dynamics of a guest/host system are the same as that of solute–solvent interactions in liquids, albeit of reduced configuration space. Moreover, the cryogenic temperatures provide a more demanding test for accurate representation of the quantum aspects of the underlying dynamics.

Our goal is to develop a direct connection between spectroscopic observables and molecular dynamics by *describing the time evolution of the quantum many-body amplitudes, while retaining the full description of the underlying nonlinear classical dynamics*. The approach will be formally developed. Here, we give an intuitively clear framework for the development, by considering progressively refined injections of quantum mechanics in an otherwise classical simulation. To this end, consider as a target the familiar correlation function, $C(t)$, which arises in linear spectroscopy

$$C(t) = \langle \psi(\mathbf{r}; 0) \psi(\mathbf{r}; t) \rangle = \left\langle \psi(\mathbf{r}; 0) \int d\mathbf{r}_0 \kappa(\mathbf{r}, \mathbf{r}_0; t) \psi_0(\mathbf{r}_0; 0) \right\rangle, \quad (1)$$

where \mathbf{r} represents the vector of all position variables, and the time evolution of the initial state, a canonical Boltzmann distribution at thermal equilibrium, is given by the propagator $\kappa(\mathbf{r}_0, \mathbf{r}, t)$.²⁹ In a strictly classical simulation, in which the swarm of trajectories plays the role of a wave packet, the propagator can be expressed as

$$\kappa_{cl}(\mathbf{r}, \mathbf{r}_0; t) = \delta[\mathbf{r} - \mathbf{r}(\mathbf{r}_0, \mathbf{p}_0; t)], \quad (2)$$

where $\mathbf{r}(\mathbf{r}_0, \mathbf{p}_0; t)$ obey classical equations of motion with initial conditions $\mathbf{r}_0, \mathbf{p}_0$. While the molecular motions are well described, what is missing in such a treatment is information about phases associated with quantum amplitudes. As a zeroth order approximation, we may consider the inclusion of phases that result from action integrals³⁰

$$\kappa^{(0)}(\mathbf{r}, \mathbf{r}_0; t) = \delta[\mathbf{r} - \mathbf{r}(\mathbf{r}_0, \mathbf{p}_0; t)] e^{-iS(t)/\hbar}, \quad (3)$$

where

$$S(t) = \int_{cl} dt \sum_j [T_j(t) - V_j(\{\mathbf{r}_j\}, t)], \quad (4)$$

where the integration is limited to classical paths, the summation j is over all particles, and the potential experienced by the j th particle is a function of coordinates of all particles. This simple fix may appear crude. Yet, it proves to be useful even at cryogenic temperatures for treating what may be regarded as bath degrees of freedom: Modes which have high thermal occupation numbers, $\bar{n} \equiv kT/\hbar\omega \gg 1$ (ω being a characteristic frequency of motion).

Missing in $\kappa^{(0)}$ is the interference among members of the trajectory ensemble, since one trajectory is propagated at a time. The exact quantum propagator is a sum over all paths, which can be thought of as a current flow through phase space.²⁹ The current density peaks on the classical path, the path that minimizes action, and decays away from it through interferences. Thus an improved approximation to the quantum evolution can be obtained by weighting the classical trajectories according to their instantaneous quantum current density at the classical path. The semiclassical Van Vleck propagator accomplishes this by assigning weights based on the curvature of the action space at the classical points.³¹ With the Van Vleck propagator cast in an initial value representation^{23–28}

$$\kappa^{(2)}(\mathbf{r}_0, \mathbf{r}, t) = \int d\mathbf{p}_0 \sqrt{\frac{d\mathbf{r}(t)}{d\mathbf{p}_0}} \delta[\mathbf{r} - \mathbf{r}(\mathbf{r}_0, \mathbf{p}_0; t)] e^{-iS(t)/\hbar}, \quad (5)$$

the weight of a trajectory is given as the sensitivity of position at time t to initial choice of momentum \mathbf{p}_0 . While this form is well suited for simulations, it requires the computation of $N^2/2$ elements of the matrix of second derivatives, and adds significant overhead if all coordinates were to be treated within the same order of approximation. As will be shown, this is not necessary. $\kappa^{(2)}$, which corresponds to second order in the stationary phase approximation of the full quantum propagator, can be shown to be exact for short times.³² $\kappa^{(0)}$ corresponds to the zeroth order in the stationary phase approximation, and can be expected to be useful for describing nearly classical degrees of freedom, modes for which $\bar{n} \gg 1$. We will show that mixed order simulations, where the bath degrees of freedom are propagated according to (3) while the solute degrees of freedom are propagated according to (5) are quite adequate for most spectroscopic applications in condensed media. Moreover, since spectroscopic observables in condensed media reflect relatively short-time dynamics, the bare propagators $\kappa^{(0)}$ and $\kappa^{(2)}$ can be used without further uniformization. This is to be contrasted with gas phase applications in which long-time propagations are required, and accordingly dressed propagators, usually frozen Gaussians,³³ are used for stability and the possibility of regenerating the time dependent wave packets. The variety of existing methods, such as the cellular method of Heller,²⁴ the Herman, and Kluk propagator²³ which involves propagation with frozen Gaussians,²⁶ the integral expressions advanced by Kay,²⁷ and the Gaussian filters suggested by Cao and Voth,²⁸ are all designed for this purpose.

We expand on the above outline in Sec. III, where we give the defining equations for implementation of the method. Since we use the spectroscopy of matrix isolated iodine as our instrument for developing the subject, in Sec. II we succinctly review the relevant experimental data and their prior theoretical treatments, and provide a more concrete exposition of the issues. To test the accuracy of the various approximations used, in Sec. IV we consider one-dimensional problems for which exact treatments are possible. The absorption and emission spectra of I₂ isolated in solid Kr are presented and analyzed in Sec. V. As an example of nonlinear spectroscopy, the RR spectra of matrix isolated I₂ will be given in Sec. VI followed by conclusions in Sec. VII.

II. SYSTEM

The visible absorption spectrum of molecular iodine, which gives it its purple color, is dominated by the $B(^3\Pi_{0u}) \leftarrow X(^1\Sigma_g^+)$ transition.³⁴ The highly structured gas phase spectrum of this transition is one of the best catalogued, used as a wavelength calibration standard.³⁵ In condensed media, for I₂ dissolved in liquids,³⁶ or solids,³⁷ the structure collapses completely, leaving a broad absorption envelope. The breadth of the absorption reflects the fact that the Franck–Condon region occurs on the repulsive wall of

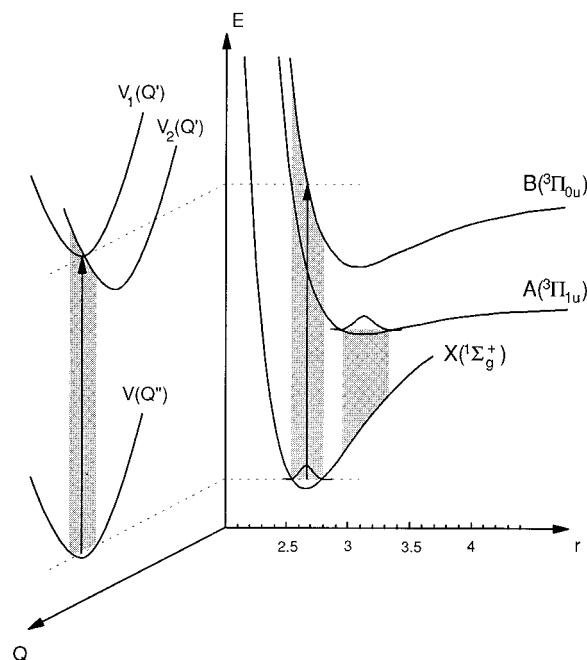


FIG. 1. The three electronic potential energy curves of I₂, which are used in the paper, are illustrated along r . The lattice potentials are illustrated by a representative coordinate Q . Zero-phonon excitation results when potentials along all lattice coordinates are identical in the ground and excited electronic states, exemplified by V_1 , while phonon sidebands will result when this does not hold, as in the case of V_2 .

the B state, spanning nearly the entire bound part of the potential and extending well into its dissociation continuum (see Fig. 1). The loss of structure is taken as an indication of “electronic dephasing” of the vertically prepared state on the time scale of 100–200 fs. In contrast, in time domain studies, when a nonstationary superposition of vibrational states is prepared in the B state, the population density is observed to preserve its coherence until predissociation, on a time scale of 5–10 ps.¹⁹ These studies establish that the B state potential parameters are preserved in matrices, and that both vibrational relaxation and predissociation are quite inefficient. Time resolved measurements on the same transition in the liquid phase are extensive.³⁸ The combination of relaxation and predissociation now occurs on a time scale of < 1 ps.³⁹

In condensed media, excitation of I₂ in the visible spectrum leads mainly to emission over the formally non allowed $A'(^3\Pi_{2u}) \rightarrow X(^1\Sigma_g^+)$ and $A(^3\Pi_{1u}) \rightarrow X(^1\Sigma_g^+)$ transitions. In rare gas matrices, this emission is structured, and the vibronic progression, although broadened, is assigned.^{37,40–42} Analysis of the Franck–Condon factors establishes that save for a ~ 200 cm⁻¹ red shift in electronic origin, the potential parameters—equilibrium bond lengths in the A/A' and X states, the harmonic frequency, and the anharmonicity of the X state—are virtually identical to that of the free molecule.^{37,41} The observed spectrum in matrix Ar was simulated by Messina and Coalson, using the time dependent Hartree method.⁴³ Good agreement with experiment was

found in this linear chain model, with the Ar lattice represented by 25 coupled harmonic oscillators.

Resonant Roman (RR) spectra of I₂ isolated in matrices,^{44–46} and in liquids such as CCl₄, Xe, and hexane,^{47,48} show progressions with as many as ~25 overtones. In addition to the coherent RR progression, a broad continuum arising from incoherent fluorescence during population relaxation is observed.⁴⁷ While the intensity distribution in the RR progression is similar in liquid and solid phases, the relative ratios of intensities in the RR progression vs the continuous background are quite different, the continuum emission being almost two orders of magnitude larger in rare gas matrices.⁴⁶ The solid state RR spectra were first analyzed by the semiclassical wave packet formalism⁵ by Kono and Lynn.⁴⁹ They accounted for the intensity distribution of the progression by incorporating a phenomenological exponential damping, which had to be adjusted to account for the excitation profile. Schwentner *et al.* have extensively discussed the RR spectra of I₂, both in liquid and solid state, with respect to their information content on ultrafast dynamics,⁴⁷ and have carried out similar one-dimensional simulations.^{47(b)} The nonmonotonic decay of intensities in the RR progression was thought to indicate that electronic predissociation plays a role on ultrafast time scales, a contention supported in recent liquid phase simulations,^{50,51} but contrary to direct measurements in the solid state.¹⁹ Quite recently, simulations of RR spectra were presented by Jungwirth *et al.* for I₂ in Ar and Xe clusters, using the method of classically-based separable potentials.⁵² In this variant of the time dependent Hartree methods, classical trajectories are first calculated, then a one-dimensional wave packet is propagated on the mean classical potential of all other degrees of freedom. Despite the approximations inherent in the averaging over dynamics, the limitation to finite size clusters, and the absence of nonadiabatic effects, the method has yielded results that are in qualitative agreement with the condensed phase experiments.⁵²

We will constrain our attention to these three spectra: The A → X emission, the B ← X absorption, and the RR scattering of I₂ isolated in solid Kr. To set the stage and the scope of the rest of the paper, we preview the issues at stake.

Consider the B ← X transition of molecular iodine, which is illustrated in Fig. 1. The correlation functions that describe the spectra in condensed media are functions of all degrees of freedom; r along I–I, and $\{Q_i\}$ along the n other coordinates. Within the Born–Oppenheimer separated Hamiltonian, the system evolves on potential energy surfaces which are also functions of all coordinates. The many-body potentials are nevertheless related to pair potentials, to I–I, I–Kr, and Kr–Kr interactions, in a yet to be specified manner. A vertical transition in which only the guest potentials change, i.e., $V(r') \neq V(r'')$ while $V(Q'_i) = V(Q''_i)$ for all Q_i , corresponds to zero-phonon (ZP) excitation.⁵³ Sharp ZP lines play an important role in solid state photophysics, and have accordingly been studied extensively.⁵³ While the description of potentials, illustrated by $V_1(Q')$ in Fig. 1, is necessary to produce ZP transitions, it is not sufficient to produce sharp lines. The potentials, through their gradients,

summarize the instantaneous forces operative upon the vertical transition, but fail to impart information about kinematic coupling. To be clear, consider the dynamics following excitation. Initially, a multidimensional wave packet which is non stationary only along r , is created. The packet soon evolves along the Q_i modes which are coupled to r . As the I–I coordinate moves toward its stretched excited state minimum, it has to push the cage atoms out of the way. The rate of momentum transfer in this process depends not only on potentials but also on masses. The heavy I atoms may displace the cage atoms in one collision, sending shock waves into the lattice.^{54,55} In contrast, if the impurity were much lighter than the host atoms, say, a hydride, then the lattice would respond sluggishly under the cumulative effect of many collisions. If the former case were to prevail, the decay of the correlation function would be complete prior to completion of the molecular vibrational period, and a structureless spectrum would result. Subject to the same potentials, in the case of the light impurity, many recursions along r would occur prior to motion along bath coordinates. This would produce a modulated correlation function, and accordingly sharp ZP lines. Clearly, even in this most favorable case for system-bath separation, the details of the dynamics dictate the spectra, and the validity of treatments under assumptions of linear response, or averaged-out dynamics, are questionable.

Even if the transition dipole were localized on the impurity coordinate, the more common case in electronic transitions is one in which potentials along bath coordinates vary with electronic states. In our example, we may expect the I–Kr interactions to depend on the electronic state of I₂, and at least the nearest neighbor I–Kr potentials to be sensitive to the sudden change in the molecular charge distribution in going from say, a Σ to a Π state. This is represented by $V_2(Q)$ in Fig. 1. Now, upon the vertical transition, the many-body wave packet will instantaneously evolve not only along r , but also along Q_i . This ballistic motion is the earliest component in solvation dynamics, to be contrasted with the picture of inertial solvation accepted in thermal liquids.^{57–59} The absorption spectrum now contains phonon sidebands, or equivalently, solute–solvent combinations modes are directly prepared. It is no longer obvious how to separate modes into system and bath. The safest route is to consider the system as a whole. Curiously enough, since the total Hamiltonian neither dissipates nor dephases, such terminologies, which are germane to treatments of reduced Hamiltonians become less meaningful. The possibility of treating the system as a whole leads us to new perspectives.

III. METHOD

We start this section by recasting the correlation function of (1) in a density matrix formalism, appropriate for thermal conditions in many-body systems. We then relate the semiclassical propagators $\kappa^{(0)}$ and $\kappa^{(2)}$ to the exact quantum propagator, using known derivations. We then introduce various methods of implementation for calculating correlation functions. We make the following assumptions through-

out: (a) the solutions are dilute such that solute–solute interactions can be neglected, (b) the electronic excitation is localized on the solute coordinate, consistent with the fact that the host is a dielectric of large band gap, (c) the Condon approximation, that the transition dipole is independent of nuclear coordinates, (d) adiabatic dynamics over Born–Oppenheimer separated surfaces prevails. For clarity, the formulation is developed in one-dimension, although the implementation is in many dimensions.

The correlation function of Eq. (1) may be cast in a more useful form

$$\begin{aligned} C(t) &= \sum_i e^{-\beta E_i} \langle \psi_i(x;0) e^{iH_g t/\hbar} e^{iH_e t/\hbar} \psi_i(x;0) \rangle \\ &= \text{Tr}[\rho_g e(x'', x'; t)] \\ &= \int dx \int dx' \int dx'' \kappa_g(x'', x; t) \rho(x'', x') \kappa_e(x', x; t), \end{aligned} \quad (6)$$

in which g and e label initial and final electronic states, and the correlation is between coherent states evolving on the excited and ground electronic surfaces. In the density matrix notation, the trace over electronic off-diagonal matrix elements is required, with the initial distribution given as the equilibrium density matrix on the initial electronic state, $\rho_{if}(x', x''; 0) = \rho_0(x', x'')$, and κ_g and κ_e are the time propagators on the ground and excited electronic surfaces. The statement is exact if we identify κ as the Feynman propagator which connects x' to x in time t along all possible paths²⁹

$$\kappa(x', x; t) = \langle x' | e^{-iHt/\hbar} | x \rangle = \int_{x'}^x D[x(t)] e^{iS(x(t))/\hbar}. \quad (7)$$

We classify the semiclassical methods according to the approximation to which the path integral is taken. After the usual discretization of paths in time, and expanding S in a Taylor series at the stationary phase:

$$S = S_{\text{cl}} + \frac{1}{2} \sum_{i,j} \frac{d^2 S}{dx_i dx_j} + \dots \quad (8)$$

if only the zeroth order in the expansion is retained, i.e., the first term in Eq. (8), the $\kappa^{(0)}$ propagator in Eq. (3) is obtained. Keeping both terms in Eq. (8), the Van Vleck propagator, is obtained^{60–62}

$$\begin{aligned} \kappa^{(2)}(x, x_0; t) &= (1/2\pi i \hbar)^{1/2} \sum \left| \frac{d^2 S}{dx_0 dx} \right|^{1/2} e^{[iS(x, x_0)/\hbar - i\nu\pi/2]} \\ &= (1/2\pi i \hbar)^{1/2} \sum \left| \frac{dp}{dx_0} \right|^{1/2} e^{[iS(x, x_0)/\hbar - i\nu\pi/2]}, \end{aligned} \quad (9)$$

where the summation is over all classical paths that lead from x_0 to x in time t ; and ν is the Maslov index which is updated by one for every zero crossing of dp/dx_0 .⁶² This is a boundary value problem, incommensurate with molecular dynamics treatments which solve for deterministic equations of motion based on initial values. For short propagations,

since trajectories may be defined either by their endpoints or by their initial conditions, we may change variables from final positions to initial momenta

$$dx = dp_0 \left| \frac{\partial x(x_0, p_0)}{\partial p_0} \right|, \quad (10)$$

to retrieve the propagator $\kappa^{(2)}$ of Eq. (5). The general expression for correlation functions can now be stated as

$$\begin{aligned} C(t) &= \int \int dx'_0 dp'_0 \int \int dx''_0 dp''_0 \int dx \left| \frac{dx'_t}{dp'_0} \right|^{1/2} \left| \frac{dx''_t}{dp''_0} \right|^{1/2} \\ &\quad \times \rho(x'_0, x''_0) e^{i(S'_{\text{cl}} - S''_{\text{cl}})/\hbar + i(\nu'' - \nu')\pi/2} \\ &\quad \times \delta(x'_t - x) \delta(x''_t - x), \end{aligned} \quad (11)$$

where the integration over all initial momenta replaces the summation over all paths. The expression (11) can in principle be evaluated by box integration over all initial conditions: x'_0 , x''_0 , p'_0 , p''_0 . There are two difficulties associated with such a procedure. First, for proper statistics a large number of initial momenta and positions should be sampled even for one degree of freedom; second, the trajectories represent delta functions and therefore the correlation integrals can only be achieved through an appropriate uniformization. These difficulties can be circumvented by taking advantage of the time reversal symmetry of classical trajectories. The trace in Eq. (6) implies that at time t only trajectories that terminate on the diagonal in the x', x'' plane contribute to the correlation function [see Fig. 2(a)]. Given time reversibility, it is possible to start from the endpoints of trajectories, i.e., from the diagonal $x'_t = x''_t$, and to allow the paths to terminate at random positions. Now, the contribution of such trajectories to the correlation function is obtained by weighting the final positions with the smooth distribution function $\rho(x'_0, x''_0)$, as shown in Fig. 2(a). This procedure already provides a significant savings in computation, and yields better statistics since the two-dimensional sampling of initial conditions required in forward-time propagation is reduced to the one-dimensional sampling of the diagonal in the x', x'' plane. The roles of start and end points are now exchanged, as indicated in Fig. 2(a). Henceforth, the subscript ₀ will imply the initial conditions for reverse-time propagation. The correlation function (11) now reduces to

$$\begin{aligned} C(t) = C(-t) &= \int \int dp''_0 dp'_0 \int dx_0 \left| \frac{dx'_t}{dp'_0} \right|^{1/2} \left| \frac{dx''_t}{dp''_0} \right|^{1/2} \\ &\quad \times \rho(x'_t, x''_t) e^{i(S'_{\text{cl}} - S''_{\text{cl}})/\hbar + i(\nu'' - \nu')\pi/2}. \end{aligned} \quad (12)$$

Note, that since the trajectories could have reached the diagonal with an unspecified momentum, in the time-reversed implementation, the limits of integration of both momentum and coordinate are from $-\infty$ to ∞ . Accordingly, the evaluation of Eq. (12) with proper statistics remains a formidable task. Quite generally, two different limits, for which practical approximations yield satisfactory results, prevail. These are the high temperature limit, where strictly classical paths are

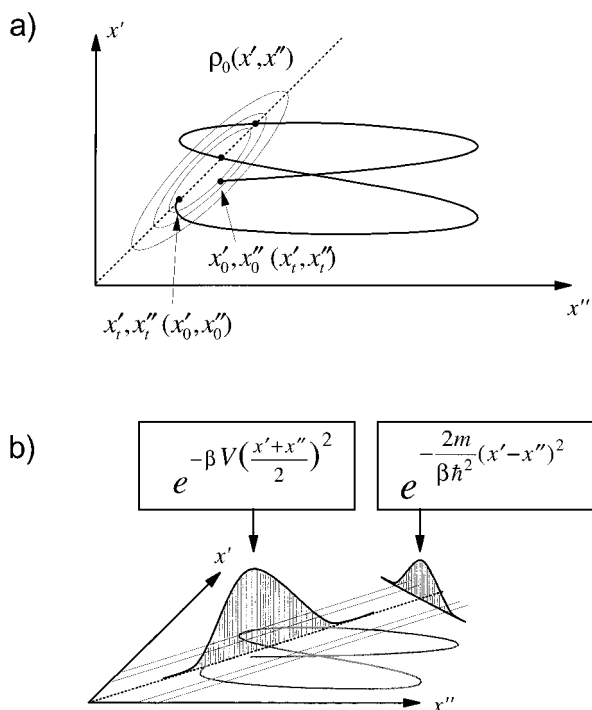


FIG. 2. (a) A typical pair of classical trajectories that contribute to the correlation function is shown in x', x'' space. In Eq. (11) each pair of trajectories is started from the arbitrary point x'_0, x''_0 that belongs to the initial distribution $\rho_0(x', x'')$ shown as contours. The trajectory contributes to the correlation function only at the crossing points with the diagonal as dictated by the delta functions in Eq. (11). The time reversed notation of Eq. (12) is shown in parenthesis. The trajectories are now started from the diagonal and correlated using the initial density $\rho_0(x', x'')$. (b) Illustration of the approximation of Eq. (15). The part of the density matrix which depends only on the average $(x' + x'')/2$ is used to filter the initial distribution of trajectories on the diagonal. The off-diagonal part is used to correlate x' and x'' for each pair of trajectories.

considered; and the zero-temperature limit, where the initial state is stationary and therefore propagation on only the final state is required.

In the high temperature limit, the contribution to the correlation function is dominated by classical trajectories. We may therefore resort to using $\kappa^{(0)}$ which is equivalent to giving unit weight to all trajectories in Eq. (12). Further, we note that only when p'_t and p''_t are similar will the correlation between the trajectories on the excited and ground state be non negligible. Accordingly, we replace the double integration over independent momenta, by a single integration over the dummy momentum p_t and use $\rho(p_0)$ as a momentum correlation function. Thus in the high temperature limit $C(t)$ reduces to

$$C(t) = \int \int dp_0 dx_0 \rho(p_0) \rho(x'_t, x''_t) e^{i(S'_{cl} - S''_{cl})/\hbar}. \quad (13)$$

The initial density matrix in the present treatment acts as the smooth function used to correlate the trajectories. The standard method of obtaining the density matrix for an arbitrary multidimensional system is by using an inverse Wigner transform of the classical phase space distribution⁶³

$$\rho_0(x', x'') = \exp\left[-\beta V\left(\frac{x' + x''}{2}\right)\right] \exp\left[-\frac{2m(x' - x'')^2}{\beta \hbar^2}\right], \quad (14)$$

where $\beta = 1/k_B T$ is the inverse temperature. Substitution of Eq. (14) in Eq. (13), changing the index in position distribution from t to 0, and regrouping terms, leads to a more transparent form for $C(t)$:

$$C(t) = \int \int dp_0 dx_0 \rho_{cl}(x_0, p_0) \times \exp\left[-\frac{2m(x'_t - x''_t)^2}{\beta \hbar^2}\right] e^{i(S'_{cl} - S''_{cl})/\hbar}, \quad (15)$$

in which the first factor acts as the filter for initial conditions, while the second factor acts as the continuous spatial function used for correlating the trajectories. The combined effects of the filter function and the correlating function illustrated in Fig. 2(b), mimic the initial statement of the problem, illustrated in Fig. 2(a). Although the approximations that led to this final form seem drastic, and while it is clear that the result converges to the correct limit as $T \rightarrow \infty$, we show in the next section that the limit of validity of Eq. (15) extends to $T \approx \hbar \omega / k_B$.

In the zero-temperature limit, since the system is initially in an eigenstate, only the final state evolves. It is now natural to think in terms of wave packets, and $C(t)$ is most directly obtained by substituting $\kappa^{(2)}$ in Eq. (1)

$$C(t) = \int \int dp_0 dx_0 \left|\frac{dx_t}{dp_0}\right|^{1/2} \psi_0(x_0) \psi_0(x_t) e^{iS_{cl}/\hbar - i\nu\pi/2}, \quad (16)$$

here x_t represents the trajectory evolving on the final state potential, beginning from the distribution given by the zero-point wave function on the initial state. The latter also plays the role of a smooth correlating function. The time dependent weights are computed using the auxiliary equation of motion

$$\frac{d^2 J}{dt^2} = -\frac{V''}{m} J, \quad \text{where } J = \frac{dx_t}{dp_0}, \quad (17a)$$

with initial conditions

$$J_0 = 0 \text{ and } m \left.\frac{dJ}{dt}\right|_0 = 1, \quad (17b)$$

where $|J|^{1/2}$ is the weight of the trajectory, and the zero crossings of J is used to update the Maslov index. Note, J is an oscillatory function. For harmonic potentials, V'' is a constant, and therefore J oscillates with a fixed amplitude. In the case of anharmonic potentials, the oscillation amplitude grows, leading to an exponential growth in the weight of a trajectory.

Equations (15) and (16) represent the final forms used in our implementation to spectral simulations in the many-body system. The guest degree of freedom, I₂ in this case, is treated through Eq. (16), while the bath degrees of freedom, ~ 100 rare gas atoms, are treated through Eq. (15). It is easy to show that Eq. (16) is exact in the case of harmonic poten-

TABLE I. Parameters used in the simulations.

Potential	Potential parameters	
	Type	Parameters (Å, cm ⁻¹)
I-I (X) ^a	Morse	$D_e=12\,550$, $x_e=2.65$, $\beta=1.871$
I-I (A) ^a	Morse	$D_e=1840$, $x_e=3.10$, $\beta=2.147$
I-I (B) ^a	Morse	$D_e=4503$, $x_e=3.016$, $\beta=1.850$
I-Kr (isotropic) ^b	LJ	$\sigma=3.74$, $\epsilon=233.5$
I-Kr (Σ) ^c	Morse	$D_e=287$, $x_e=3.733$, $\beta=1.49$
I-Kr (Π) ^c	Morse	$D_e=126$, $x_e=4.30$, $\beta=1.540$
Kr-Kr ^b	LJ	$\sigma=3.58$, $\epsilon=199.5$

^aReference 64.^bReference 65.^cMorse fit to parameters given in Ref. 66.

tials. In anharmonic potentials, both expressions are only valid for short times. Yet, the time scale over which the correlation functions retain accuracy is sufficiently long for our application. In his introduction of the cellular method, the recognition that the initial value Van Vleck propagator is accurate for times longer than previously thought has been the important discovery by Heller,²⁴ as pointed out by Miller.²⁵ Since our prescriptions rely on the bare propagators, we establish the limits of their validity prior to implementations.

IV. IMPLEMENTATION IN ONE-DIMENSIONAL SYSTEMS

We test the limits of validity of both zero-temperature and high-temperature approximations of $C(t)$ given in Sec. II, by considering the $A \rightarrow X$ emission and the $B \leftarrow X$ absorption spectra of free iodine, the same transitions which will later be treated in the many-body system. The Morse potential parameters used in these simulations are given in Table I.

A. The $A \rightarrow X$ emission at 0 K

We evaluate Eq. (16) by identifying $\psi_0(x_0)$ as the vibrational ground state of the $A(^3\Pi_{1u})$ electronic state of iodine. The classical trajectories, x_t , their weights, $|dx_t/dp_0|^{1/2}$, and the associated classical actions, S_t , are computed on the final state of the transition, the $X(^1\Sigma_g^+)$ ground electronic state. Initial positions and momenta are chosen from a uniform 40×40 grid. The limits of integration over initial positions is well defined, suffice that they encompass $\psi_0(x_0)$. The limits of integration over initial momenta must include a representative ensemble of trajectories that contribute to the correlation function through final positions. The range of relevant momenta depends on the target time. At early time, although the dynamics is uninteresting, the number of contributing trajectories is large. This can be understood by noting that the relevant range of integration in momentum space is given as

$$\Delta p \sim \Delta x / \Delta t, \quad (18)$$

where Δx is the width of ψ_0 . Despite the fact that as $t \rightarrow 0$ the number of contributing trajectories diverges as $1/t$, since the weights of trajectories are zero at $t=0$ and grow as t at early time, the resulting correlation function is well behaved.

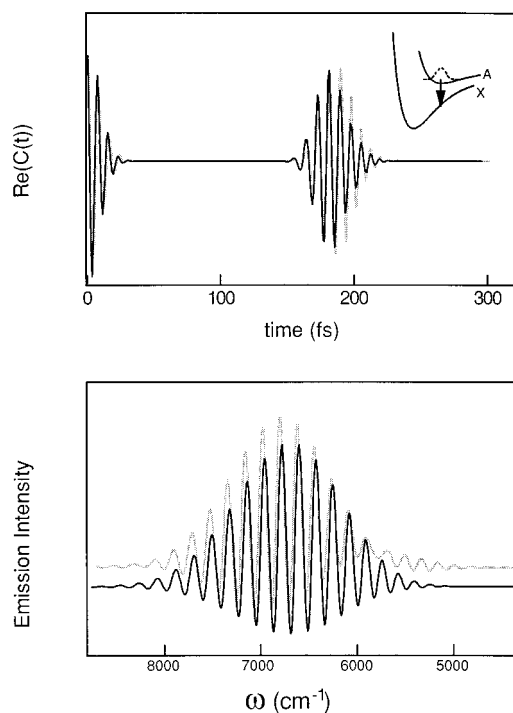


FIG. 3. The correlation function (top panel) and the spectrum (lower panel) of the $A \rightarrow X$ emission of gas phase iodine: (gray line) calculated using the second order semiclassical propagator, Eq. (16) of text; (black line) exact solution obtained by wave packet propagation. The semiclassical calculation involves the propagation of 4×10^4 trajectories for the first 5 fs and 10^4 trajectories for the remaining 300 fs.

In order to obtain accurate values for the correlation function at the first time step, $t = \Delta t = 1$ fs in our case, it is necessary to sample an initial momentum range of $p_{\max} = -p_{\min} = \mu \Delta x / \Delta t$. In nearly harmonic potentials it is useful to keep the full set of trajectories to allow a sharp definition of later rephasings. However, quite generally, in anharmonic potentials and for relatively short propagation times, it is possible to discard a large fraction of these trajectories without compromising the accuracy of the correlation function.

The computed correlation function for the $A \rightarrow X$ transition is shown Fig. 3(a). A total of 4×10^4 trajectories were propagated in the first 5 fs, and 10^4 trajectories were retained for the subsequent 500 fs. The fact that there is no discontinuity in $C(t)$ at 5 fs ensures that we have not removed any contributing trajectories. The number of trajectories can be reduced to as low as 800 for $t < 5$ fs and 160 for $t > 5$ fs without a significant effect on signal-to-noise ratio when only early time dynamics, $t < 0.5$ ps, is of relevance. Indeed, as we will see, this is the time scale of relevance in the condensed phase.

A comparison of the semiclassical correlation function, and the resulting spectrum obtained by its Fourier transform, with those of an exact quantum calculation, is shown in Fig. 3. The exact solution is obtained by wave packet propagation, by solving the time dependent Schrödinger equation using the now standard FFT algorithms.⁶⁷ The comparison is

quite satisfactory. The correlation functions, which are illustrated for the time of completion of the first recursion, show deviations due mainly to discarding 80% of the initial trajectory ensemble. The effect of this on the spectrum is rather subtle, appearing as small deviations at the high frequency end. Note, the spectral resolution is dictated by the propagation time of 1 ps, and the negative intensities in the spectrum are the result of boxcar apodization in the Fourier transform.⁶⁸

B. The A→X emission at finite temperature

Next, we consider the low temperature limit of validity of correlation functions constructed according to Eq. (15), which is based strictly on $\kappa^{(0)}$, and should generally be valid at high temperatures. We consider the same spectrum as above, but now for $T=150$ K ($\hbar\omega/2k_B=60$ K in the A state). The initial conditions for the trajectories, x_0 and p_0 , are now obtained by Monte Carlo sampling of the classical phase space distribution

$$\rho_{cl} = \exp\left[-\beta\left(V(x) + \frac{p^2}{2m}\right)\right]. \quad (19)$$

For a given choice of x_0 , p_0 , a pair of trajectories is propagated, one on the A potential and one on the X. The pairs are then correlated according to Eq. (15). The spectrum, generated from a swarm of 300 pairs of trajectories propagated for 1 ps, is shown in Fig. 4. For comparison, the exact stick spectrum is also shown. Progressions arising from the thermal populations in $v=0,1,2$ in the A state, are clearly evident in both spectra. The comparison is quite impressive given the conceptual simplicity of the method: Correlation of classical trajectories that carry phases given by action integrals over classical paths.

Next we consider an initial temperature, $T=10$ K, where the classical phase space distribution is unphysical. The results of the simulation are shown in Fig. 5, along with the exact stick spectrum. The proper Franck–Condon envelope is retrieved, and the vibrational spacing in the central part of the spectrum is correct. However, the anharmonicity in the wings of the spectrum is not reproduced. This failure is to be understood by noting that the classical swarm evolving on the X state represents the vibrational superposition that would have been created by a vertical projection of the initial distribution on the A state (shaded area in Fig. 1). Since at 10 K the classical distribution is significantly narrower than the quantum zero-point distribution, a tighter superposition composed of only few members in the central part of the packet is simulated by the swarm. That the envelope is accurately represented is due to compensation of the correlating function $\exp[-2m(x' - x'')^2/\beta\hbar]$ in Eq. (15) for the contraction of the initial distribution [see Fig. 2(b)]—the position-momentum uncertainty is retained. This feature of the thermal correlation (15) makes it well suited for treating bath degrees of freedom.

For a one-dimensional systems, the unphysical situation considered above can be avoided by using the quantum den-

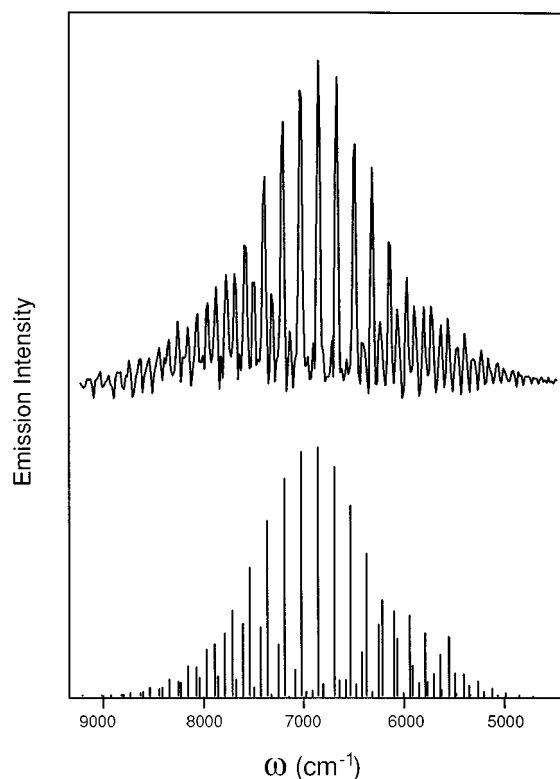


FIG. 4. The gas phase spectrum of the A→X emission of iodine at 150 K. The top spectrum is obtained using the zeroth order propagator, Eq. (15) of text, by propagating 300 pairs of trajectories for 1 ps. The stick spectrum is obtained by using exact frequencies and Franck–Condon factors of the vibrational eigenstates on the excited and ground potential energy surfaces.

sity matrix of an oscillator in contact with a thermal bath,⁶⁹ by using the scaled temperature, T_{cl} , in Eq. (19)

$$T_{cl} = \frac{\hbar\omega}{2k_B} \left[\tanh\left(\frac{\hbar\omega}{2k_B T}\right) \right]^{-1}, \quad (20)$$

where ω is the harmonic frequency of the initial state, and T is the real temperature. Note that now, when $\hbar\omega \sim k_B T_{cl}$, contributions to the spectrum from vibrationally excited initial states will appear. Indeed the A→X thermal simulation with $T_{cl}=60$ K is essentially indistinguishable from the exact $T=0$ K spectrum. It should be cautioned that this fix cannot be rigorously implemented in many-body systems, say by Monte Carlo sampling from normal modes at different scaled temperatures. Such an artificial initial distribution will lead to unphysical time evolution since initially the system is not at classical equilibrium. Instead, as in our previous simulations of solid state dynamics, we resort to a scaled temperature based on the Debye frequency of the lattice.^{18,19}

C. The B←X absorption at 0 K

The time scale over which Eq. (16) retains its accuracy depends on the extent of anharmonicity of potentials. The reason for this is well understood.⁷⁰ Since in anharmonic potentials the weight of a given trajectory grows exponentially with time, conservation of total flux implies that at long times few trajectories represent the entire packet—the major-

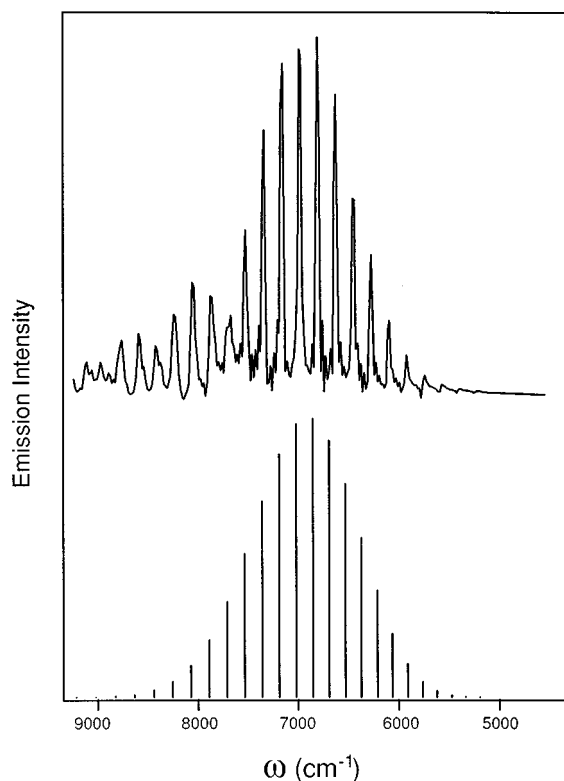


FIG. 5. The gas phase spectrum of the $A \rightarrow X$ emission of iodine at 10 K. The top spectrum is obtained using Eq. (15), by propagating 300 pairs of trajectories for 1 ps. The stick spectrum is obtained by using exact frequencies and Franck–Condon factors of the vibrational eigenstates on the excited and ground potential energy surfaces.

ity of the members of the swarm cancel out through destructive interference. The fewer the working trajectories the poorer is the representation of the wave packet. In the case of the $A \rightarrow X$ transition, although the final state is a Morse potential, the vertical transition terminates deep in the X potential where anharmonicity is relatively small. In contrast, the $B \leftarrow X$ absorption involves a transition that straddles the dissociation limit of the final state. Part of the initial packet is projected into the continuum, and part remains in the bound region (see shaded region in Fig. 1). This extreme of anharmonicity provides a rigorous test of the time scale of validity of the bare semiclassical treatments.

The zero-temperature $B \leftarrow X$ absorption spectrum using Eq. (16) is shown in Fig. 6. The details of the calculation are the same as in the $A \rightarrow X$ treatment, except the number of trajectories is now augmented by an order of magnitude. The greater number of trajectories is needed to accurately reproduce the dynamics up to $t = 1$ ps. Judging from spectra obtained by transforming the time correlation function for ever increasing time scales, it is possible to conclude that the first 800 fs of the dynamics is accurately reproduced. This corresponds to the termination of the first recursion (see Fig. 6). When a longer segment of the time file is Fourier transformed, an artificial modulation of the spectrum appears. In order to reproduce the nodal pattern after the first recursion, and to continue the simulations for subsequent periods, it is

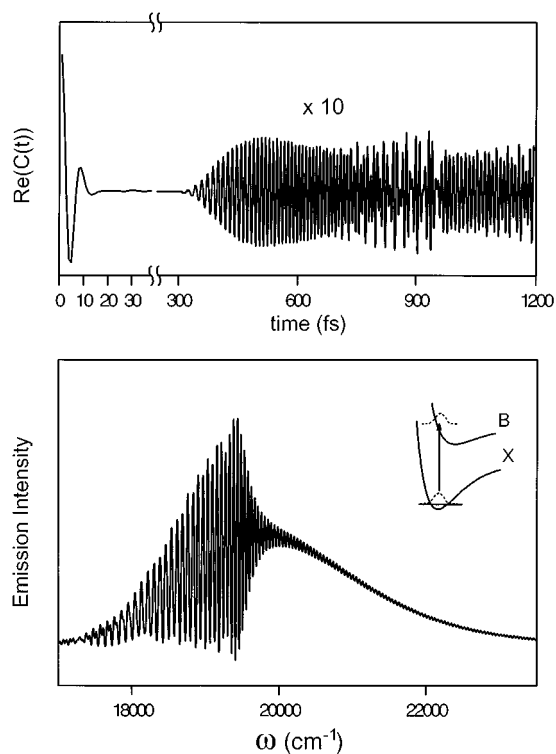


FIG. 6. The correlation function (top panel) and the spectrum (lower panel) of the $B \leftarrow X$ absorption of gas phase I₂ calculated by the semiclassical method [Eq. (16) in text]. The calculation involves the propagation of 6.4×10^5 trajectories for the first 5 fs and 1.28×10^5 trajectories for the remaining 1.2 ps.

necessary to regenerate the wave packet. For this transition, the correlation function in the initial 300 fs can be accurately calculated by using as few as 800 trajectories for the first 5 fs and 160 trajectories after that.

D. The $B \leftarrow X$ absorption at finite temperature

The computed correlation function and the spectrum of the $B \leftarrow X$ transition with the high temperature method (15), are presented in Fig. 7. The initial conditions were chosen from a thermal distribution at 80 K, at which the classical phase space distribution approximates the quantum zero-point distribution on the X state. The initial decay of the correlation function, which gives rise to the correct Franck–Condon envelope, is reproduced. On the other hand, the method fails to reproduce the structure of the spectrum below the dissociation limit. This marks the limitation of the strict use of $\kappa^{(0)}$. The interferences in the evolving wave packet, which produce the structure in the spectrum, is not adequately represented. Also, spectral congestion due to absorption from $v = 1$ occurs. The higher resolution required to sort out the different progressions requires several periods of motion on the initial state for which methods based on bare propagators fail. Note, the differences between this case and that of the $A \rightarrow X$ transition are the extent of the nonlinearity of dynamics, and the higher frequency of the oscillator in the final state. This clearly shows the necessity of propagating such modes through $\kappa^{(2)}$.

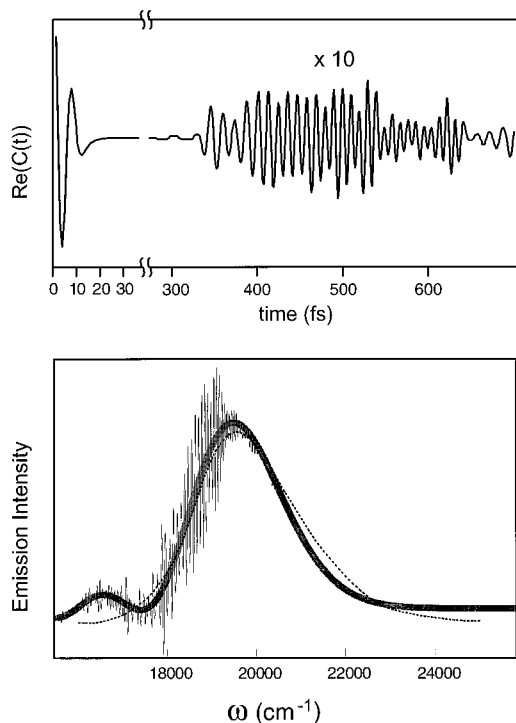


FIG. 7. The correlation function (top panel) and the spectrum (lower panel) of the $B \leftarrow X$ absorption of gas phase iodine at 50 K. The thin line and thick gray line are the spectra obtained using Eq. (15), by propagating 300 pairs of trajectories for 800 and for 100 fs, respectively. The dashed line is the spectrum obtained by the classical reflection approximation.

V. MANY-BODY SPECTRA

The spectral simulations of I₂ isolated in a matrix of Kr are carried out in mixed order: I₂ is treated in second order in the $T=0$ K approximation, the lattice atoms are treated in zeroth order, with an initial thermal density at the scaled temperature of 45 K (Debye temperature = 72 K).⁶⁵ The initial conditions are obtained by Monte Carlo sampling, and the classical trajectories are propagated using molecular dynamics.⁷¹ A cell of 108 Kr atoms, subject to periodic boundary conditions, is used. I₂ is placed in a double substitutional site created by the removal of a nearest neighbor pair of Kr atoms. Lennard-Jones potentials are used to describe Kr–Kr interactions, and Morse potentials are used to describe I–I interactions in the various electronic states. First, we consider zero-phonon (ZP) absorption and emission spectra by using the same I–Kr potentials in the initial and final electronic state (see Sec. II). In these simulations, as in the prior simulations of pump–probe observables,^{18,19} the I–Kr interactions are modeled by Lennard-Jones potentials suitable for Xe–Kr (see Table I). We then consider a treatment in which the I₂–Kr potentials depend on the electronic state of I₂, by constructing the three-body potential from the anisotropic I–Kr fragments.^{66,72,73} This construct is described in the Appendix, along with the justification for using isotropic pair potentials in the excited state. The need for using anisotropic potentials to describe the ground state has already been demonstrated in the analysis of the spin–orbit transition of atomic iodine isolated in solid Kr and Xe.⁷⁴

These electronic state dependent potentials allow a natural treatment of non-ZP-transitions, and consideration of the effect of instantaneous forces along guest–host coordinates.

The initial conditions for the simulations are sampled in the following manner: The I₂ coordinate is selected from a grid that spans its $v=0$ wave function, the I₂ momenta are sampled randomly from a box distribution; the Kr coordinates and momenta are sampled from a thermal lattice equilibrated about the particular state of the guest by interrupting a thermal simulation of the initial state. Then, for a given set of initial conditions, a pair of trajectories are propagated, one on the initial state and one on the final state. The classical action associated with each coordinate is computed, as well as the time-dependent weight of trajectories along the I–I coordinate according to Eq. (17). To construct the many-body correlation functions, first, the pairs of trajectories are correlated: The I₂ trajectory on the final state is correlated with its initial state stationary wave function according to Eq. (16) and the Kr trajectories are correlated according to Eq. (15); then, the ensemble average is constructed by summing over all trajectories

$$C(t) = \frac{1}{N} \sum_{\text{traj}} \left[\langle R_{I_2}(t) R_{I_2}(0) \rangle \prod_i \langle R_{Kr,i}(t) R_{Kr,i}(0) \rangle \right. \\ \left. \times e^{i(S_X - S_A)/\hbar} \right] = \left\langle \mathcal{E}_{I_2}(t) \prod_i \mathcal{E}_{Kr,i}(t) \right\rangle_T, \quad (21)$$

in which $\langle \dots \rangle_T$ denotes the ensemble average of N trajectories, and $\mathcal{E}(t)$ is used to designate the correlation for a pair of trajectories. The spectra are obtained by Fourier transforming $C(t)$ and weighting the transform by ω or by ω^3 in case of absorption or emission, respectively.

A. The $A \rightarrow X$ emission in solid Kr

A total of 400 pairs of trajectories were propagated for 800 fs to simulate the I₂ ($A \rightarrow X$) transition. The real part of the calculated $C(t)$ and the associated emission spectrum are shown in Fig. 8. The spectrum, its envelope and widths of individual vibronic lines, are in good agreement with the published experimental spectra in solid Kr.^{37,43} While the agreement is gratifying, the more valuable aspect of the treatment is the possibility to decompose the many-body correlation function into its constituent contributions. This is done in Fig. 9, in which, in addition to $\text{Re}[C(t)]$, we also show the ensemble averages of the I₂ position correlation function, $C[r_{I_2}(t)]$, the collective bath (lattice) position correlation function, $C[R_B(t)]$, and the position correlation function of a nearest neighbor Kr atom lying along the molecular axis, $C[R_{Kr}(t)]$. These real functions are defined as

$$C[r_{I_2}(t)] = \langle \langle R_{I_2}(t) R_{I_2}(0) \rangle \rangle_T, \quad (22a)$$

$$C[R_B(t)] = \left\langle \prod_i \langle R_{Kr,i}(t) R_{Kr,i}(0) \rangle \right\rangle_T, \quad (22b)$$

$$C[R_{Kr}(t)] = \langle \langle R_{Kr}(t) R_{Kr}(0) \rangle \rangle_T. \quad (22c)$$

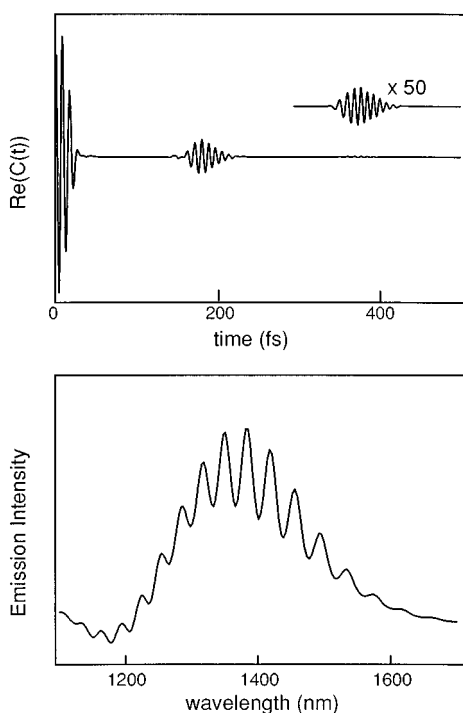


FIG. 8. The correlation function (top panel) and the spectrum (lower panel) of the $A \rightarrow X$ emission for I₂ isolated in solid Kr.

These are nearly classical measures, in that they do not include phase information. With this decomposition of $C(t)$, we proceed to interpret the spectrum of Fig. 8 in terms of the molecular mechanics.

The envelope of the emission spectrum in Fig. 8 contains no information about the many-body dynamics. The width of the envelope of $\sim 1000 \text{ cm}^{-1}$ is determined by the initial decay in $C(t)$, which is complete at $t \sim 25 \text{ fs}$. During this period, the collective bath correlation remains constant, as seen in Fig. 9, while along the I₂ coordinate, the wave packet ballistically moves out of the Franck–Condon region. This is, in part, by design. Since a strictly ZP transition is being considered, at $t=0$ the only active force is along the I–I coordinate. Indeed, it is difficult to distinguish the first decay in $C(t)$, the first 50 fs, of the free molecule from that of the molecule embedded in the solid (compare Figs. 3 and 8), with the consequence that their spectral envelopes are nearly identical. A careful comparison of $\text{Re}[C(t)]$ shows that in the many-body simulation the modulation is slightly damped due to the ensemble averaging, or equivalently due to the cross correlation among the members of the trajectory ensemble. This effect is rather small, leading to an almost unnoticeable broadening of the spectrum by $\sim k_B T$. Figure 9 also illustrates that the initial decay in $C[R_{I_2}(t)]$ lags behind $C(t)$. This is a realization of the fact that for an anharmonic potential the phase velocity of the packet is faster than its group velocity. *The quantum correlation function is a time-dependent measure of the joint momentum-position overlap between the initial and final states.* This initial decay results from the loss of overlap as the packet moves out of the

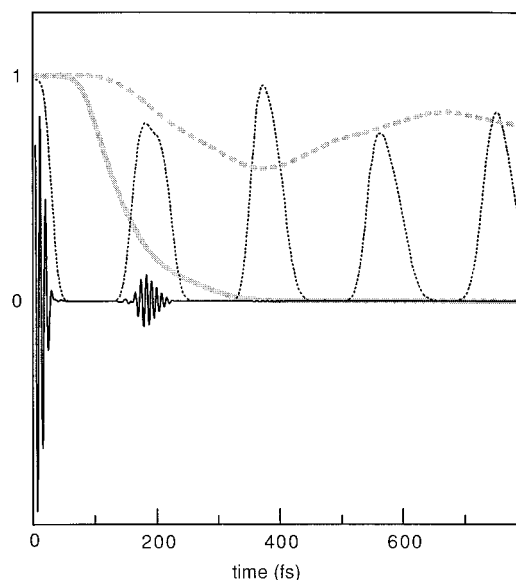


FIG. 9. Decomposition of the correlation function for the $A \rightarrow X$ emission of I₂ isolated in solid Kr: Solid black line—the real part of the supersystem autocorrelation function, $\text{Re}[C(t)]$; dashed line—the I₂ position autocorrelation function, $C[R_{I_2}(t)]$; solid gray line—the collective bath position autocorrelation, $C[R_B(t)]$; dashed gray line—the position autocorrelation function of an individual Kr atom, $C[R_{Kr}(t)]$.

Franck–Condon region. Since we have developed our formalism in position representation, the momentum correlations are mainly formed in the ensemble averaging of phases, or in the cross correlation among trajectories. To move, the packet needs to develop momentum, which it does by conversion of potential into kinetic energy; and the path integral of the momentum forms the phase of the packet. Since the noise due to thermal initial conditions is much smaller than the momentum derived from the steep difference potential gradient, the momentum correlations survive the ensemble averaging. In this ballistic phase of dynamics the packet evolves coherently, without scrambling of the momentum-position correlations. The initial decay is not permanent. The structure in the spectrum is the result of the fact that the supersystem, molecule and host, will rephase twice prior to complete loss of correlation (see Fig. 9).

Information on the many-body dynamics is contained in the individual vibronic line shapes in the spectrum of Fig. 8. If we characterize the vibronic lines by only a width, then this would be determined by the permanent decay time of $C(t)$. Note that this decay is not the result of energy redistribution. It can be seen in Fig. 9 that the I₂ position correlation shows nearly complete recursions at every $\sim 200 \text{ fs}$. The amplitude of these recurrences, which is a measure of the I₂ vibrational energy content, decays only by $\sim 10\%$ on the simulation time scale of 1 ps. Nevertheless, $C(t)$ decays to zero near the third recurrence, near $t=400 \text{ fs}$, and the spectrum does not contain any information past this time. Figure 9 makes it clear that the permanent decay of $C(t)$ is the result of correlation loss in the collective bath coordinate, in $C_B(R(t))$. By choice of potentials, a system–bath separation can be made for this case, where the supersystem corre-

lation function is given as the product of the free molecule correlation and the bath correlation

$$C(t) = C_{I_2}(t) \left\langle \prod_i \mathcal{E}_{Kr,i}(t) \right\rangle_T = C_{I_2}(t) C_{Bath}(t). \quad (23)$$

Now, $C_{I_2}(t)$ acts as a function that samples $C_{Bath}(t)$ with a characteristic period of 200 fs. The sampling period is, however, too long for a detailed measure of the bath correlation function. Only two recursions survive, the bath correlation function is only sampled twice prior to complete decay, and therefore a variety of approximate expressions may reproduce the line shape. It may, for example, be possible to make the stochastic ansatz for $C_{Bath}(t)$ of a Gaussian decay at early time, and an exponential decay at later time, to reproduce the line shape. Yet, this would neither fit the simulated function nor would it contain the proper physics. The function is described by an initial nearly flat induction period of ~ 100 fs, a sudden decline near 200 fs, followed by a decaying tail that extends to 400 fs. These stages of the loss in the bath memory correspond to the inertial period, coherent excitation transfer and redistribution, steps that can be entirely understood by the underlying molecular mechanics.

Consideration of the typical host atom correlation function is helpful in understanding the mechanism of the bath decay. First, we note that while the collective memory decays, any one atom may show partial coherence and will maintain a terminal nonzero correlation. The depicted atom in Fig. 9 suffers a head-on collision at the completion of the first period of motion by I₂ on the X surface, while during the first 200 fs it is nearly unaffected by the ongoing dynamics. In the initial state the system was at equilibrium on the A surface, in which the I₂ equilibrium bond length, $R_e = 3.1$ Å, is substantially longer than that on the final X state, $R_e = 2.7$ Å. Thus, upon the vertical transition from A to X, the oversized initial cage cavity gently implodes on I₂(X). The depicted Kr atom is set into a sluggish motion initially and suffers a gentle collision only after I₂ stretches out to the original Franck–Condon region, at $t = 200$ fs, i.e., after a full period of nearly harmonic motion along I–I on the X surface. This collision deflects the Kr atom outwards, such that at $t = 400$ fs, the molecule can fully stretch and a nearly complete recursion occurs in the I₂ position correlation. The process repeats, and the Kr correlation settles to ~ 0.75 , indicating that the final lattice relaxation is minor and that the single atom position density retains significant overlap with its original value. The decay of the bath correlation is simply the result of there being many such partially displaced atoms. To see this, let us make the assumption of separability, which is certainly valid at long time

$$C[R_B(t)] = C[R_{Kr}(t)]^n, \quad (24)$$

in which n is the effective number of participants in the bath, i.e., the effective number of Kr atoms that behave as the depicted atom. At $t = 400$ fs, when the I₂ position correlation is nearly 1, and the single Kr atom correlation, although at a minimum, has a significant value of $C[R_{Kr}(t)] = 0.6$; assuming $n = 10$, the bath correlation function would be predicted

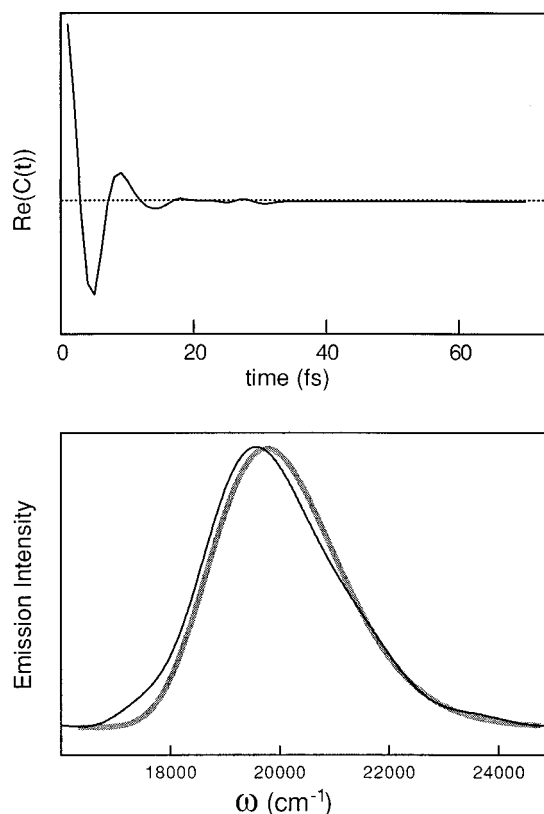


FIG. 10. The correlation function (top panel) and the spectrum (lower panel) of the $B \leftarrow X$ absorption of I₂ isolated in solid Kr ($T_{cl} = 45$ K). The classical reflection approximation for the same spectrum is shown with the thick gray line in the lower panel. The shift in maxima of the two spectra is the result of solvation in the matrix.

to decay to 6×10^{-3} , which is close to the observed value. Thus, the overall decay can be understood in terms of the dimensionality of the problem, the result of the displacement of many atoms in the dynamics. An analysis of the time dependent number of participants (or coupled modes) is useful in constructing statistical models, its deduction from (24) hinges on separability of coordinates, an issue to which we return below. The main points from the above are: The signature of the many-body dynamics is contained in the spectral line shapes of the individual vibronic lines, which are mainly determined by the functional form of the decay of the collective memory in positions, $C[R_B(t)]$. Moreover, the bath correlation function is not a simple decay.

B. The $B \leftarrow X$ absorption in solid Kr

With initial conditions sampled from a lattice equilibrated around I₂(X), we propagate trajectories in pairs, now, on the X and B surfaces. A total of 400 pairs of trajectories were propagated for 1 ps, and the correlation functions were constructed as above. $\text{Re}[C(t)]$ and the associated spectrum for the $B \leftarrow X$ transition in solid Kr are shown in Fig. 10. As in the experiments, a structureless spectrum which is well approximated by the nondimensional classical reflection, is obtained. The comparison shows that as a result of solvation, relative to the free molecule spectrum, the many-body spec-

trum is redshifted by $\sim 200 \text{ cm}^{-1}$. This is consistent with experimental estimates of the reduction in electronic origin.⁴² A decomposition of the correlation function, shown in Fig. 11, indicates that in this case, as the wave packet moves out of the Franck–Condon region, the many-body correlation decays to zero prior to recursion along the I–I coordinate, and does not recover. In contrast with the $A \rightarrow X$ transition, which leads to a gentle cage implosion, in this case the cage is driven out along an explosive coordinate. The nonlinearity of the dynamics is quite clear from the I₂ position correlation, the first recursion of which now occurs with a large dispersion in time stretching from 350 to 1000 fs. This should be contrasted with the nearly harmonic motion along the I₂ coordinate in the case of the $A \rightarrow X$ transition shown in Fig. 9. Now, it is not possible to establish a meaningful value for the characteristic time of energy flow from the molecule to the lattice. Trajectories initiated near the dissociation limit lose their energies instantaneously, while those in the bound region decay on the time scale of many picoseconds, as demonstrated in time domain studies.¹⁹ The nonlinearity of dynamics is more severe for the portion of the packet created above dissociation, as already described in detail through the analysis of similar dissociative trajectory data.¹⁸ This very efficient energy transfer has no direct signature in the spectrum.

Due to the very steep gradient on the B state, the initial decay in $C(t)$ due to the ballistic stage of motion along I₂, occurs within ~ 10 fs. In this period the free molecule and many-body correlation functions are indistinguishable (compare $\text{Re}[C(t)]$ in Figs. 6 and 10). The spectral envelope contains no information about environmental effects. The environmental effect is the loss of structure in the spectrum, which results from the decay of the bath correlation function to zero upon the first stretch of the I–I bond, near 200 fs, prior to the first recursion along I–I, which starts at 350 fs. Although the simulation fixes the bath decay at $t=200$ fs, based on the experimental spectrum we can only establish that this occurs sometime between 20 and 350 fs. The origin of this rapid decay in the overall correlation is strictly mechanical. Due to the large mass of the I atoms, the nearest neighbor atoms faithfully respond to the stretch of the I₂ bond in the B state. The cage deforms, and the bath correlation function permanently decays due to the loss of overlap in position density. A nearly classical treatment of the dynamics would have been sufficient to reproduce this spectrum.

The decomposition of Fig. 11 shows that the individual Kr position correlation contains a coherence dip, and does not decay to zero. Its terminal value settles at ~ 0.4 , implying a large permanent displacement. This is sufficient to destroy the overall correlation function because of the number of participants in the displacement. The number of Kr atoms that are typified by the depicted neighbor may be extracted according to Eq. (24) from the logarithmic ratio

$$n(t) = \frac{\ln\{C[R_B(t)]\}}{\ln\{C[R_{Kr}(t)]\}}. \quad (25)$$

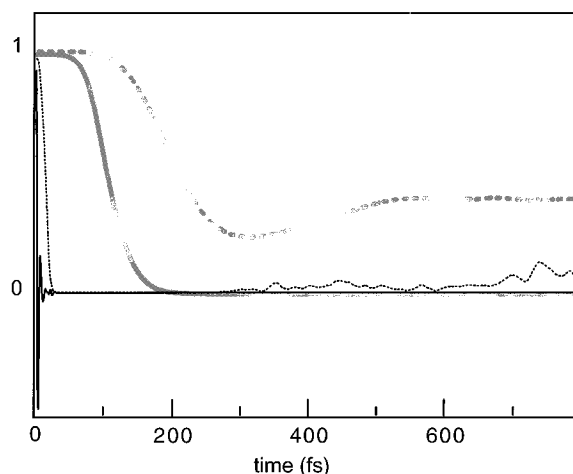


FIG. 11. Decomposition of the correlation function for the B – X absorption of I₂ in solid Kr: Solid black line—the real part of the supersystem autocorrelation function, $\text{Re}[C(t)]$; dashed line—the I₂ position autocorrelation function, $C[R_{I_2}(t)]$; solid gray line—the collective bath position autocorrelation, $C[R_B(t)]$; dashed gray line—the position autocorrelation function of an individual Kr atom, $C[R_{Kr}(t)]$.

Note, this analysis hinges on the separability of coordinates, on the assumption that the many-body correlation function is the product of correlation functions of individual coordinates. The choice of “good” coordinates, ones that are separable, is crucial for applications such as time dependent Hartree treatments. However, as all model treatments of many-body dynamics, the validity of approximations are difficult to test. We can address this issue here, through various decompositions of the data. The nonseparability arises from the fact that the ensemble average of coupled degrees of freedom is not the product of ensemble averages

$$\left\langle \prod_i C[R_{Kr,i}(t)] \right\rangle_T \neq \prod_i \langle C[R_{Kr,i}(t)] \rangle_T. \quad (26)$$

A plot of $n(t)$ vs t is shown in Fig. 12, along with the quantities in the inequality of Eq. (26). The inequality is particularly severe at early times, where nonsensical values of $n > 100$ are observed [see Fig. 12(a)]. At later time, where the Kr atoms are set into large amplitude motion, the assumption becomes sensible. The coherence minimum, near 350 fs, involves only 5 to 6 cage atoms. They represent the atoms which are overdriven by the stretching I₂ molecule, and which bounce back after hitting the second solvent shell. At long time, $n(t)$ reaches a constant value of 18, which corresponds to the number of nearest neighbors in a double substitutional site, and represent the number of atoms that are permanently displaced. With the terminal value of the single atom correlation of 0.4, the bath correlation decays to 7×10^{-8} . Figure 12(b) makes it clear that the inequality of Eq. (26) persists throughout the simulated dynamics, however, the differences past the first 200 fs are not significant, only because the magnitude of $C(t)$ is now very small. Thus the assumption of separability is poorest at the earliest time, where small amplitude but collective coordinates of the bath

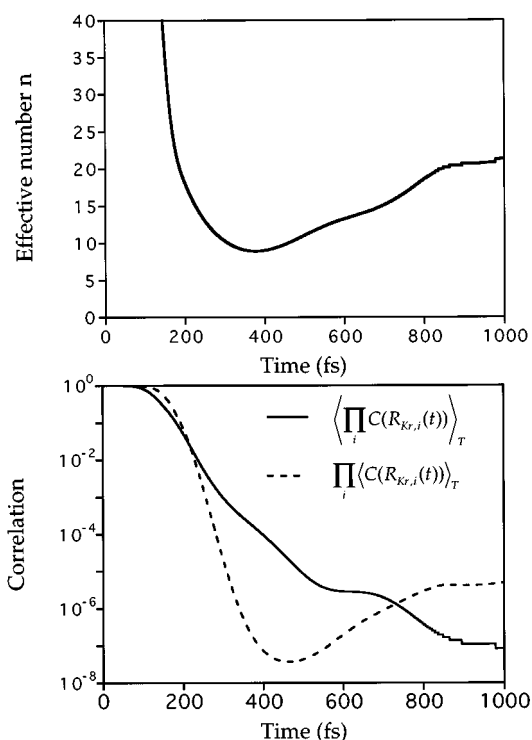


FIG. 12. Effective number of participants, n of Eq. (23) in text, is shown in the top panel, and the inequality of Eq. (26) is shown in the lower panel.

are excited. Upon stretching the cage coordinate, which has previously been identified as the E_g mode, past its harmonic amplitude, the packet along this coordinate splits into many independent components, and a picture of isolated atomic motions becomes the more useful coordinate to consider. The first crossover point from collective dynamics to isolated atomic motions, or the breakup of the cage packet, coincides with the decay of the bath correlation function near 200 fs.

What role do phases play in shaping the spectrum? To address this issue, in Fig. 13 we compare the bath position autocorrelation, $C_B[R(t)]$ defined with the exclusion of phases in Eq. (22b), with a decomposition of the complex bath correlation function:

$$C_B(t) = \left\langle \left(\prod_j \langle R_{Kr}(t) R_{Kr}(0) \rangle_j \right) \exp \left\{ i \sum_j [S_{B,j}(t) - S_{X,j}(t)] t / \hbar \right\} \right\rangle_T \quad (27)$$

into its real and imaginary parts [the index j in Eq. (27) runs over all Kr atoms]. The real part of the bath correlation shows a partial phase coherence, as evidenced by the damped oscillations and the anticorrelation (the negative portion of the function before it returns to zero). Inclusion of phases leads to a structured bath correlation, and a somewhat faster initial decay. The imaginary part of the function clearly shows that phases develop with the transfer of momentum from the stretching I₂ to the bath. Since the initial guest–host impact parameters are strictly from a thermal distribution, the ensemble averaging effectively damps the phase coher-

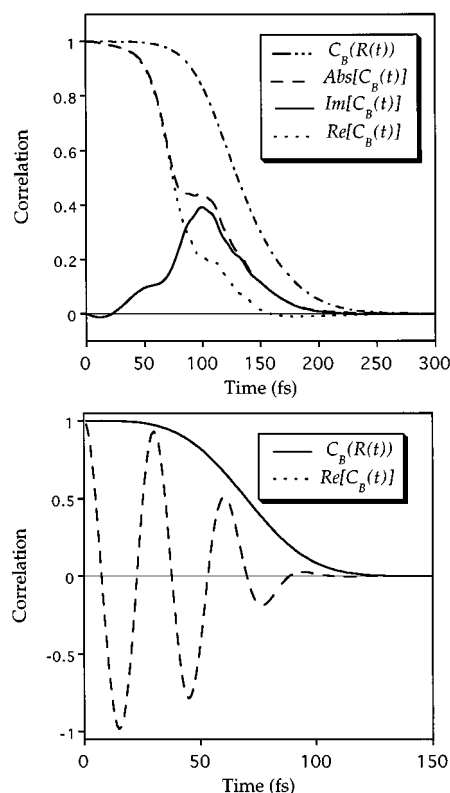


FIG. 13. Decomposition of the bath correlation function for the $B \leftarrow X$ transition showing the role of phases. Top panel—zero-phonon excitation, with a decomposition of the complex autocorrelation function, $C_B(t)$, and the position autocorrelation, $C_B[R(t)]$. The difference between these two functions is the result of ensemble averaging of phases. Bottom panel—nonzero-phonon excitation, the complex autocorrelation and the position autocorrelation nearly follow each other.

ence in the bath. Note, however, the final decay to zero in $|C_B(t)|$ and $C_B[R(t)]$ coincide near $t \sim 250$ fs. Once again, the position correlation function, or the displacement of the nearest neighbors, leads to the permanent decay. The origin of this behavior is also mechanical in nature. In the ZP excitation, as the I–I bond starts to stretch, initially some momentum develops on the nearest Kr atoms. Soon afterward, the I atoms start pushing their neighbors against the lattice potential, and no kinetic energy develops during this displacement not until the recoil of the I atoms. Upon their recoil, the cage atoms are repelled by the lattice, and now for the first time they evolve freely and develop momentum. At the recoil stage, the momenta come into play, and momentum redistribution in the bath can potentially play an important role in determining the correlation function. In this case, the loss of position autocorrelation preempts this role.

C. The non-zero-phonon $B \leftarrow X$ absorption

Using the same methodology as above, we simulate the $B \leftarrow X$ absorption in solid Kr, but now using the potential construct described in the Appendix. In the excited electronic state, the same potentials as before are used. However, the initial conditions are sampled from the ground state in which the anisotropic Kr–I₂ potential is used. The difference in

excited and ground state potentials along the I–Kr coordinate now implies that the vertically created wave packet is subject to forces not only along I–I but also along I–Kr coordinates. Nevertheless, the initial decay in $C(t)$ is dominated by the ballistic evolution along I–I, since the gradient of the difference potential, $\nabla(V_B - V_X)$, along the internal coordinate of the guest is much larger than along the guest–host coordinates. The first 20 fs of $C(t)$ is identical to the ZP case, accordingly the spectrum is identical. Experimental absorption spectra cannot distinguish between these two cases. The collective bath correlation is shown in Fig. 12(b), to be compared with the ZP-excitation case. The decay in $C_B[R(t)]$ is now complete in ~ 120 fs, the system memory is shortened by a factor of in comparison to the ZP case. The real part of the complex bath correlation function now shows a strictly coherent phase evolution. Its decay is controlled by the position autocorrelation of the bath. The phase coherence survives the ensemble averaging, since it too is strictly the result of the ballistic motion along the guest–host coordinate. Quite clearly, a system–bath separation along a guest–host division is inappropriate in this case. Presumably, a better choice of coordinates in terms of normal modes of the difference potential, could lead to a more reasonable separation. However, as we pointed out above, as the dynamics evolves the separable coordinates will also evolve. Such considerations are of no consequence in the present treatment. The dominant mechanism for the decay of correlations remains the same: The loss of position autocorrelation, $C_B[R(t)]$, affected by the impulsively initiated plastic deformation of the cage. The shortening of memory in this case is simply the result of the difference potential topology. In the ground state there now are minima along the collinear approach. As a result, Kr atoms are localized along the immediate line of impact, and the collision time is shorter than before.

VI. MANY-BODY RESONANT RAMAN SPECTRA

According to the Kramers–Heisenberg expression for Raman scattering,⁷⁵ the Raman process with excitation resonant with the $B \leftarrow X$ transition, can be regarded as: Optical excitation from $X(v=0)$ in a thermal lattice to the B state, time evolution of the system on the B surface, and radiation of the evolving density back to the X state. The spectrum can then be constructed as a three-time correlation function.⁷⁶ This would be accomplished in the present method by propagating a pair of trajectories on both excited and ground surfaces, then, at finite time intervals, allowing the excited state trajectory to spawn new trajectories on the ground state the continuing propagation on both excited and ground states. The Fourier transform of the triple correlation, after ensemble averaging, yields the RR spectrum. While the recipe is clear, the execution of this procedure is computationally intensive. Now, instead of the 400 pairs of trajectories used for the simulation of the linear spectra, if 100 trajectories were spawned by the excited state trajectory, 80 000 trajectories would be required to generate the RR spectrum. While this is feasible by virtue of the relatively short time scales required to generate the coherent Raman spectra, here, we

will forego the line shape information contained in the full treatment and be satisfied by the integrated intensities under the lines. To this end, it is sufficient to project the excited state density on final scattering states, the vibrational eigenstates of I₂, without considering further time evolution on the final state.

As before, the mixed order simulations are used, and the RR spectrum for scattering into the I₂($v=n$) eigenstate is evaluated as

$$\begin{aligned} I(\omega_n) &= \omega_n^3 \omega \sum_k e^{-\beta E_k} \left| \int e^{i\omega t} \langle \psi'_k(R, \{r_i\}; t) | \psi''_n(R) \right. \\ &\quad \left. \times \psi''_k(\{r_i\}) \rangle dt \right|^2 \\ &= \omega_n^3 \omega \left| \int e^{i\omega t} \text{Tr}[\rho_n(R', R'', \{r'_i, r''_i\}; t)] dt \right|^2 \\ &= \omega_n^3 \omega \left| \int e^{i\omega t} C_n(t) dt \right|^2. \end{aligned} \quad (28)$$

In effect, it is assumed that in the terminal X state, the I₂ and Kr wave functions are separable. The initial state for time propagation is now given as

$$\rho_n(R', R'', \{r'_i, r''_i\}; 0) = \psi_0(R') \psi_n^*(R'') \rho_0(\{r'_i, r''_i\}). \quad (29)$$

We first carry out the simulations for ZP excitation. Thermal initial conditions for Kr coordinates are sampled, and $v = 0$ of I₂ is used for the distribution along the I–I coordinate. Pairs of trajectories are then propagated and correlated as in the thermal absorption simulations, but now the evolving packet along the I₂ coordinate is projected on the stationary vibrational eigenstates of the molecule. A total of 5000 pairs of trajectories are used in these calculations to reproduce the correlation functions for the final scattering channels.

In Fig. 14 we show $C_n(t)$, the RR correlation function for scattering into the n th vibrational state of matrix isolated I₂. As the wave packet evolves on the excited state, it develops correlations with the X state vibrations. An important aspect to note from these plots is the spread in time over which correlations with high overtones last. For example, while the correlation for the fundamental RR peak decays in 20 fs, scattering into the tenth overtone starts near $t=0$ and decays near $t=50$ fs. The 50th overtone has a correlation function that starts near $t=20$ fs and decays near $t=150$ fs, prior to decay of the bath correlation. The correlation function for the 80th overtone starts at $t \sim 40$ fs, and terminates at $t \sim 160$ fs. The latter limit is determined by the decay of the bath correlation (see Fig. 13). The nonlocality in space and time of scattering into high overtones implies that observation of a given transition does not lead to a sharp determination of either the location of the evolving wave packet or the timing of the event. Thus, while the *RR scattering samples the full history of the quantum many-body time correlation, the sampling is coarse grained.*

The relative intensities within an overtone progression is the more useful quantity to compare with experiment. These are illustrated in Fig. 15, as a function of excitation wave-

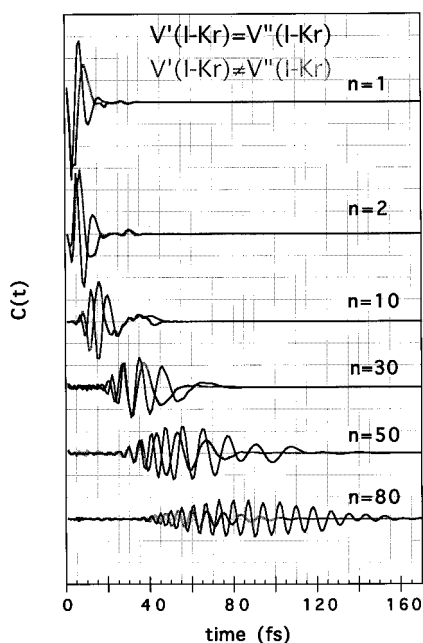


FIG. 14. Resonant Raman correlation functions, $\text{Re}[C_n(t)]$, for scattering into the n th vibrational level of I₂ isolated in solid Kr.

length. The peak of the absorption spectrum in the simulation occurs at $19\,500\text{ cm}^{-1}$, at which wavelength a slow decay in the progression intensities is observed. A sharp break in the progression occurs when the excitation is far from the band center, in preresonant, $\omega < 18\,000\text{ cm}^{-1}$, and post-resonant, $\omega > 22\,000\text{ cm}^{-1}$, spectra. As the excitation energy is raised above the absorption maximum, at $\omega > 21\,000\text{ cm}^{-1}$, the intensities in the progression show modulation. Such modulations observed in the experiments have been suspected to originate from a partial recurrence of the excited state wave packet.³⁴ This is not the case. As already discussed in the $B \leftarrow X$ absorption, the correlation of the system decays much before any recursion can occur. The modulation arises from internal diffraction due to momentum resonances between the evolving packet and the nodal pattern on the excited vibrational eigenstates in the X potential. This appears at high excitation energies, where the packet acquires a large momentum immediately upon moving away from the potential wall. Observation of internal diffraction in the gas phase is usually limited to bound \leftrightarrow free transitions, where the evolution on one surface is strictly transient.^{77,78} While it should also be present in transient preparations of bound-bound transitions, unless gated on an ultrafast time scale, this modulation would be masked by the Franck-Condon pattern of stationary states. Quite striking is also the result that overtones up to $v = 80$ are predicted to be observable, although it is to be expected that these high lying overtone transitions will be broad due to the short coherence time of the final states. Experiments show overtones up to $v \sim 25$. This discrepancy may suggest that the assumption of zero-phonon excitation is a poor one.

The simulations were repeated using the electronic state dependent I-Kr potentials described in the Appendix. The

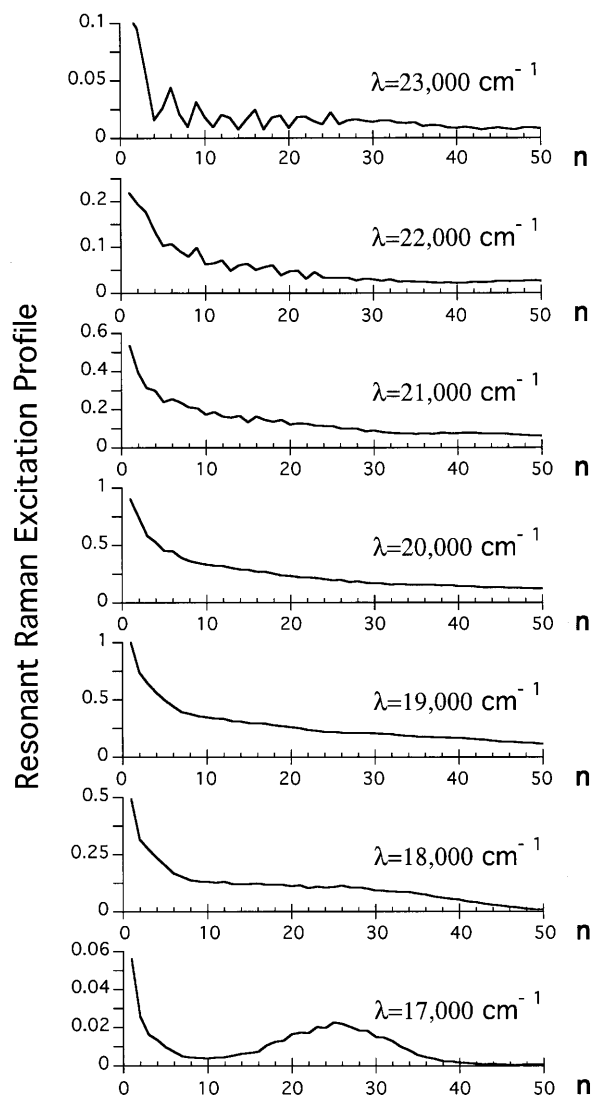


FIG. 15. Intensities of resonant Raman progressions as a function of excitation wavelength.

correlation functions obtained are directly compared with the ZP spectra, in Fig. 14. As already discussed, the bath correlation function now decays sooner, at $t = 120\text{ fs}$ as compared to 250 fs in the case of ZP excitation (see Fig. 13). While this produces the desired effect, only intensities of RR overtones above $v = 30$ are reduced. A comparison of the predicted progression intensities by the two different treatments and recently obtained experimental data is shown in Fig. 16 for excitation wavelengths of 488 and 514 nm. The predictions of the simulations are quite similar for overtones $n < 14$, and in good agreement with experiment. Both treatments deviate from the experiment for overtones 15–22, overestimating the intensities in the 514 nm data while underestimating them in the 488 nm data. Such a deviation would be expected if the red shift of the $B \leftarrow X$ absorption were overestimated. Thus, if the absorption maximum were closer to 488 nm, and therefore 514 nm were significantly further from the peak, then a softer decay of intensities would result in the former, and a

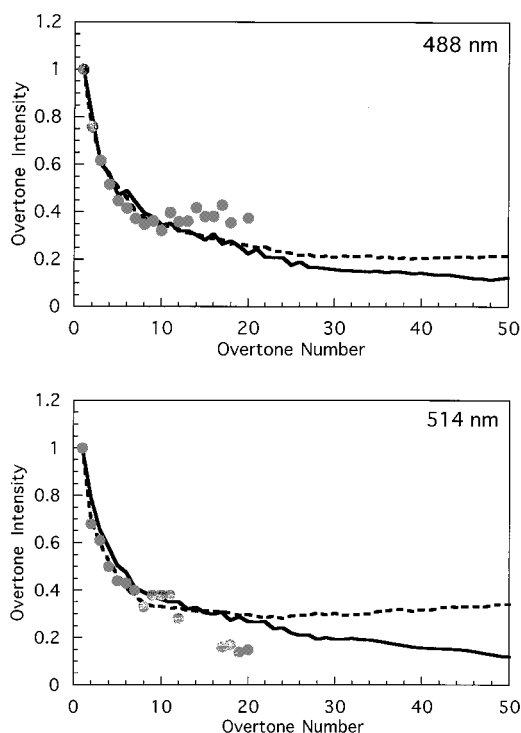


FIG. 16. Comparison of the experimental and calculated overtone intensities in the Resonant Raman spectrum of I₂ isolated in solid Kr. Circles represent the experimental results. The dashed line is zero-phonon transitions, the solid line is the non-ZP-transition obtained using the potentials in the Appendix.

steeper decay would result in the latter (see Fig. 15). Indeed, the absorption profile of I₂ is distorted from what would be expected based on the $B \leftarrow X$ transition alone, due to the contribution from the $B''(^1\Pi_u) \leftarrow X$ absorption. At 488 nm, the absorptions to B and B'' are comparable, while at 520 nm the B state absorption is ~ 4.7 times stronger than that of B'' .³⁴ Both states are Raman active, and population will evolve on both. Given the similarity of the repulsive walls of the B and B'' potentials, the dynamics on the short time scales relevant to RR would be expected to be similar. However, due to their shifted spectra, the RR excitation profiles from the different surfaces will be different. A correction strictly due to the shift in the electronic absorption maximum, would improve the agreement between simulation and experiment. Contrary to the conclusions, based on approximate analyses,⁴⁷ and in agreement with the recent conclusions of the simulations by Jungwirth and Gerber,⁵² neither predissociation nor recursions need be invoked to match the data within experimental error. However, a quantitative treatment should necessarily consider contributions from the B and B'' surfaces.

Finally, even in the nonzero-phonon excitation treatment, the RR progression is predicted to contain intensity up to $\nu = 50$. The experiments show an apparent sudden termination near $\nu = 25$ (see Fig. 16). Given the discussion of the nonlocality of the RR scattering process, it can categorically be stated that the sudden termination of the progression is unphysical. We believe that higher overtones simply

broaden, now due to the reduction of coherence times in the final vibrational states, and blend with the incoherent fluorescence background. We reserve a more quantitative analysis of experiment *vis-à-vis* theory to the future, here, we suffice by introducing the computational method and by noting its qualitative agreement with experiments, without adjustment of parameters.

VII. CONCLUSIONS

We have outlined a semiclassical method for directly connecting spectral observables to molecular dynamics in many-body systems, appropriate for treating spectroscopy in condensed media. The method relies on the simultaneous use of the bare, initial value, semiclassical propagators, $\kappa^{(0)}$ and $\kappa^{(2)}$ (the Van Vleck propagator), in constructing correlation functions that correspond to particular observables. Efficient and practical implementation of the method is possible with two approximate constructs of linear correlation functions, from which others can be pieced together. These are the zero-temperature approximation, Eq. (16), and the high temperature approximation, Eq. (15), which are appropriate for treating modes of low and high occupation numbers, respectively. The limits of validity of these constructs were demonstrated in one-dimensional treatments to be quite broad. Then the mixed order simulations were successfully applied to the spectroscopy of the prototypical system of matrix isolated I₂. In this application, it was sufficient to propagate only the I₂ internal coordinate using $\kappa^{(2)}$, while the 106 host atoms are propagated using $\kappa^{(0)}$. Propagation of all degrees of freedom with the Van Vleck propagator would be computationally intensive, since now, the weights calculated through Eq. (17) would require the evaluation of the Hessian matrix at each time step. Such a treatment is seldom necessary. Usually, based on thermal occupation numbers, it should be possible to breakdown a system into two subsets for the mixed-order treatment, to enable simulations of condensed phase systems, or large molecules, in an intuitively obvious way and without sacrificing dynamical details. The shortcoming of the method in its present form is its limitation to short time, or to low resolution spectroscopy, since the number of required trajectories scale exponentially with time. This can in principle be remedied by frequent regenerations of the evolving wave packets, by now propagating Gaussians as opposed to delta functions. The practicality of this approach in many-body systems remains to be shown.

There are many different theoretical approaches for treating spectroscopy, or quantum dynamics, in condensed media: The generalized Bloch equations of Redfield,⁷⁹ the generalized two-level systems coupled to a bath or the spin-boson formalism,⁸⁰ the time dependent self-consistent methods,^{43,52,81} methods based on mixed quantum/classical simulations,⁸² Green's function methods in state representation,⁸³ and time propagation of centroids⁸⁴ are among the examples. By nature of the problem these are all approximate methods, invariably based on treating the quantum mechanics of a small subsystem accurately, and introducing the rest of the system in an average way: Through an

influence functional, or coupling to a bath with its characteristic spectral density.⁶ Such reductions are highly useful, however, in treating real systems it is difficult to assess the validity of the approximations made in the abstractions. The reductions also define the language for describing the observables. For example, the all familiar terminology of dephasing and dissipation in describing spectral line shapes in condensed media, are derived from the Bloch equations, in which the subsystem is coupled to a bath through phenomenological decays of the off-diagonal coherence, and the diagonal population. Adherence to such language generates unnecessary confusion as illustrated by the discussions about relative magnitudes of T_1 and T_2 even in systems subject to microscopically reversible dynamics.⁸⁵ The presented formulation enables treating the system as a whole, and directly ties the observables to the fundamental molecular properties of interatomic forces. In a strict sense, the supersystem neither dephases nor dissipates, rather, after an initial preparation of a coherence, phases and energies redistribute. For systems prepared far from equilibrium, the early stages of the redistribution proceed via highly specific motion through phase space, and only in the later stages does the picture of randomization—of phases, energies, or correlations—becomes meaningful. Spectra measure the initial stages of the evolution of the coherence, through quantum correlations which represent the joint position-momentum overlap between the initial and the time evolving state. For an initial preparation far from equilibrium, only the ballistic stage of motion in phase space is measured. This stage of “solvation” will usually be governed by highly nonlinear dynamics, a language absent in most treatments, but one that emerges naturally in the present semiclassical approach.

Several important lessons are learned from the analysis of the spectra of matrix isolated I₂. The broad structureless absorption band in the $B \leftarrow X$ transition commonly invokes the notion of ultrafast electronic dephasing. This is not the case. The spectrum could have been reproduced through nearly classical molecular dynamics, i.e., with the neglect of phases but by proper inclusion of initial distributions and ensemble averages. The information content in this spectrum is quite limited, the absence of structure simply implies that the many-body correlation function decays prior to any recursion along the I–I coordinate, sometime between 20 and 350 fs. In frequency domain spectroscopy, this is the condition for validity of the classical Franck principle. In time domain spectroscopy, the same limit can be reached by using pulses shorter than any dynamical recurrences in the system, which is the key to successful simulations of ultrafast pump–probe observables through classical simulations.²² The rapid decay of the quantum correlation in this transition is the result of loss in position overlap of the cage atoms driven by the stretching I₂ bond. This is a kinematic effect. Subject to the same forces, if a light impurity were considered, we would expect significantly more structure in the bound part of the excited state potential. This indeed is the case, for example, for the $B \leftarrow X$ transition of matrix isolated Cl₂, where a structured vibronic progression with well resolved

phonon sidebands are observed near the Franck–Condon origin.⁸⁶

The $A \rightarrow X$ emission provides an interesting contrast with the $B \leftarrow X$ absorption, now the transition is to a strictly bound final state, the molecule oscillates with very slow energy flow to the lattice, and the molecular position density shows many recursions. The supersystem correlation however decays after the second recursion, a result of there being many participants in the ungoing dynamics. This is a case where dissipative quantum dynamics may be a good picture, and in fact the treatment of Messina and Coalson through the time dependent Hartree method provides a corroboration for this analysis.⁴³ Yet, the bath correlation is not a simple decay, it consists of a flat induction period, in origin equivalent to inertial solvation,^{56–59} followed by a decline representative of ballistic motion in phase space, followed by a tail that can be fitted to an exponential. The latter stage is associated with the engagement of many particles in the ongoing dynamics, close to a picture of randomization in phase space. Due to the low frequency of the I₂ oscillator, only the decaying portion of the function is sampled by $C(t)$ and hence little error is made in analyzing the spectral line shapes by Lorentzians or voigt profiles. There simply is not enough information in the experimental absorption and emission spectra to construct the correct bath correlations.

The situation is quite different in RR spectra, which sample the full evolution of $C(t)$, and the reproduction of RR progressions may be regarded as the true test of the treatment. Calculation of $C_n(t)$, the correlation function for scattering into the n th overtone, shows that inversion of spectra to obtain information about correlation functions, and therefore underlying dynamics, should be practiced with caution since due to the spread in space and time of $C_n(t)$ extensive convolution occurs. Based on approximate analyses, the RR spectra of I₂ in condensed media have been interpreted to contain signatures of ultrafast nonadiabatic dynamics.⁴⁷ Our analysis, in accord with those of Jungwirth and Gerber,⁵² shows that based on intensities in the RR progressions, there is no need to invoke nonadiabaticity. The same has also been shown in time domain measurements in solids,¹⁹ with important differences between solid and liquid phase dynamics.⁸⁷ The main difference between liquid and solid state RR spectra is the ratio of the sharp-to-diffuse intensities, and the spectral composition of the diffuse background.⁴⁶ A quantitative analysis of these details is left for the future.^{46(b)}

ACKNOWLEDGMENTS

The support by AFOSR, under a University Research Initiative grant F49620-1-0251, is gratefully acknowledged. The UCI Office of Academic Computing, and the Institute for Surface and Interface Science, are acknowledged for the allocation of computer resources.

APPENDIX

The I–Kr pair potentials have been characterized by molecular beam scattering measurements.^{66,72} The interaction is anisotropic due to the open shell structure of atomic iodine.

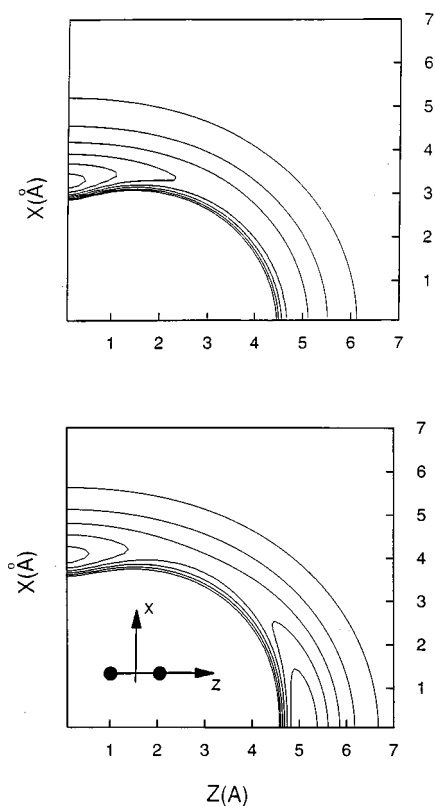


FIG. 17. Potential contours of I₂-Kr interaction, with z defined as the molecular axis. (a) Isotropic Lennard-Jones I-Kr pair potentials used for the simulations of the excited state I₂(B)-Kr interactions; (b) anisotropic I-Kr potentials used in the simulation of the ground state I₂(X)-Kr interactions (see the text). The spacing between contour lines of 50 cm⁻¹. The well depths on the ground surface are 310 and 266 cm⁻¹ for linear and T geometries, respectively. The well depth on the excited state is 321 cm⁻¹.

Based on the orientation of the p hole relative to the internuclear axis, the interaction will belong to Σ or Π representations under $C_{\infty v}$. Since Kr is a closed shell atom, the I-Kr interaction is dominated by dispersion at long distance and electron-electron repulsion at short distance. Accordingly, a deeper potential arises in the Σ approach, where the electron density is minimal along the internuclear axis. While the experiments measure spin-orbit coupled surfaces, in a strictly $l=1$ basis set (p_x, p_y, p_z), the Σ and Π contributions can be uniquely decomposed.⁷³ A rather simple construct of I₂-Kr potentials is possible in this basis set. The ground X(¹ Σ_g^+) state of I₂ arises from the overlap of p_z orbitals. Thus, with the p holes locked along z on both I atoms, the I₂-Kr interaction can be expressed as

$$V(I_2(X) - \text{Kr}) = \cos^2(\theta_1)V_{\Sigma}(r_1) + \cos^2(\theta_2)V_{\Sigma}(r_2) + \sin^2(\theta_1)V_{\Pi}(r_1) + \sin^2(\theta_2)V_{\Pi}(r_2), \quad (\text{A1})$$

where the subscripts refer to the two iodine atoms, and the angles are measured from the principle axis of the molecule.

In the excited B(³ Π_{0u}^+) state, and for I₂-Kr contained in the x, z plane, the molecular orbitals are a spatial superposition

$$\psi_{I_2}(\Pi) = \frac{1}{\sqrt{2}}(p_{1,z} + p_{2,x}) + \frac{1}{\sqrt{2}}(p_{1,x} + p_{2,z}). \quad (\text{A2})$$

Accordingly, the interaction potential is now isotropic

$$V(I_2(B) - \text{Kr}) = \frac{1}{2}[V_{\Sigma}(r_1) + V_{\Pi}(r_1)] + \frac{1}{2}[V_{\Sigma}(r_2) + V_{\Pi}(r_2)]. \quad (\text{A3})$$

The latter consideration is the justification for our prior use of pairwise additive Lennard-Jones potentials in simulating the excited Π states of I₂ in rare gas solids.^{18,19} Since we are interested in the qualitative effect of nonzero-phonon excitations, we leave the excited state potential as before, namely using Xe-Kr pair parameters. However, in treating the ground state we use Eq. (A1) with Morse fits to the experimental V_{Σ} and V_{Π} potentials (see Table I for parameters).

Contour plots of the ground and excited state potentials used in the present treatment are shown in Fig. 17. Note the difference in topologies. In the ground state the potential energy surface has comparable minima in both linear and T geometries (well depths of 290 and 266 cm⁻¹, respectively). In the excited state the minimum occurs only in the T geometry (well depth of 321 cm⁻¹).

¹M. Lax, J. Chem. Phys. **20**, 1752 (1952).

²R. Kubo and Y. Toyozawa, Prog. Theor. Phys. **13**, 160 (1955).

³R. G. Gordon, Adv. Mag. Reson. **3**, 1 (1968).

⁴E. J. Heller, Acc. Chem. Res. **14**, 368 (1981).

⁵S.-Y. Lee and E. J. Heller, J. Chem. Phys. **71**, 4777 (1979).

⁶U. Weiss, *Quantum Dissipative Systems* (World Scientific, Singapore, 1993).

⁷R. Kubo, Adv. Chem. Phys. **15**, 101 (1969).

⁸T. Takagahara, E. Hanamura, and R. Kubo, J. Phys. Soc. Jpn. **43**, 802, 811, 1522 (1977); **44**, 728, 742 (1978).

⁹S. Mukamel, J. Chem. Phys. **71**, 2884 (1979).

¹⁰S. Mukamel, J. Chem. Phys. **82**, 5398 (1985); Y. J. Yan and S. Mukamel, Phys. Rev. A **41** 6485 (1990).

¹¹S. Mukamel, *Principles of Nonlinear Optical Spectroscopy* (Oxford University Press, New York, 1995).

¹²A. E. Johnson and A. B. Myers, J. Chem. Phys. **102**, 3519 (1955).

¹³A. E. Johnson, S. Mukamel, and A. B. Myers, J. Am. Chem. Soc. **116**, 11039 (1994).

¹⁴A. E. Johnson and A. B. Myers, J. Phys. Chem. **100**, 7778 (1996); J. Chem. Phys. **104**, 2497 (1996).

¹⁵T. Joo, J. Yiwei, J.-Y. Yu, J. L. Lang, and G. R. Fleming, J. Chem. Phys. **104**, 6089 (1996).

¹⁶See, for example, W. P. Deboeij, M. S. Pshenichnikov, and D. A. Wiersma, Chem. Phys. Lett. **253**, 53 (1996); **247**, 264 (1995); **238**, 1 (1995); for a most recent exposition of theoretical thought on the subject, see L. W. Unger and J. A. Cina, Adv. Chem. Phys. (to be published).

¹⁷R. M. Stratt and M. Cho, J. Chem. Phys. **100**, 6700 (1994); B. M. Ladanyi and R. M. Stratt, J. Phys. Chem. **99**, 2502 (1995).

¹⁸Z. Li, R. Zadoyan, V. A. Apkarian, and C. C. Martens, J. Phys. Chem. **99**, 7453 (1995); R. Zadoyan, Z. Li, C. C. Martens, and V. A. Apkarian, J. Chem. Phys. **101**, 6648 (1994); R. Zadoyan, Z. Li, P. Ashjian, C. C. Martens, and V. A. Apkarian, Chem. Phys. Lett. **218**, 504 (1994).

¹⁹R. Zadoyan, M. Sterling, and V. A. Apkarian, J. Chem. Soc. Faraday Trans. **92**, 1821 (1996).

²⁰Z. Li, J. Y. Fang, and C. C. Martens, J. Chem. Phys. **104**, 6919 (1996).

²¹J. W. Che, M. Messina, K. R. Wilson, V. A. Apkarian, Z. Li, C. C. Martens, R. Zadoyan, and Y. J. Yan, J. Phys. Chem. **100**, 7873 (1996).

²²M. Sterling, R. Zadoyan, and V. A. Apkarian, J. Chem. Phys. **104**, 6497 (1996).

²³M. F. Herman and E. Kluk, Chem. Phys. **91**, 27 (1984); E. Kluk, M. F. Herman, and H. L. Davis, J. Chem. Phys. **84**, 333 (1984).

²⁴E. J. Heller, J. Chem. Phys. **94**, 2723 (1991).

- ²⁵W. H. Miller, *J. Chem. Phys.* **95**, 9428 (1991).
- ²⁶A. R. Walton and D. F. Manolopoulos, *Chem. Phys. Lett.* **244**, 448 (1995).
- ²⁷K. G. Kay, *J. Chem. Phys.* **101**, 2260 (1995); **100**, 4377, 4432 (1994).
- ²⁸J. Cao and G. V. Voth, *J. Chem. Phys.* **104**, 273 (1996).
- ²⁹R. Feynman and Hibbs, *Quantum Mechanics and Path Integrals* (McGraw-Hill, New York 1965).
- ³⁰W. H. Miller, *Adv. Chem. Phys.* **25**, 69 (1974).
- ³¹J. H. Van Vleck, *Proc. Natl. Acad. Sci.* **14**, 178 (1928).
- ³²See, for example, the discussion in Ref. 25.
- ³³E. J. Heller, *J. Chem. Phys.* **75**, 2923 (1981).
- ³⁴J. Tellinghuisen, *J. Chem. Phys.* **76**, 4736 (1982).
- ³⁵S. Gerstenkorn, P. Luc, and R. Vetter, *Rev. Phys. Applique* **16**, 529 (1981).
- ³⁶R. J. Sension and H. L. Strauss, *J. Chem. Phys.* **85**, 3791 (1986).
- ³⁷M. M. Macler, J.-Ph. Nicolai, and M. C. Heaven, *J. Chem. Phys.* **91**, 674 (1989).
- ³⁸A. C. Harris, J. K. Brown, and C. B. Harris, *Annu. Rev. Phys. Chem.* **39**, 341 (1988).
- ³⁹D. E. Smith and C. B. Harris, *J. Chem. Phys.* **87**, 2709 (1987).
- ⁴⁰P. B. Beecken, E. A. Hanson, and G. W. Flynn, *J. Chem. Phys.* **78**, 5892 (1983).
- ⁴¹R. Bohling, J. Langen, and U. Schurath, *Chem. Phys.* **130**, 419 (1989).
- ⁴²M. M. Macler and M. C. Heaven, *Chem. Phys.* **151**, 219 (1991).
- ⁴³M. Messina and R. D. Coalson, *J. Chem. Phys.* **90**, 4015 (1988).
- ⁴⁴W. F. Howard and L. Andrews, *J. Raman Spectrosc.* **2**, 447 (1974).
- ⁴⁵J. Grzybowski and L. Andrews, *J. Raman Spectrosc.* **4**, 99 (1975).
- ⁴⁶(a) V. A. Apkarian, in *Femtochemistry: Ultrafast Chemical and Physical Processes in Molecular Systems*, edited by M. Chergui (World Scientific, Singapore, 1996), p. 603; (b) K. Kizer, M. Ovchinnikov, and V. A. Apkarian (in preparation).
- ⁴⁷(a) J. Xu, N. Schwentner, S. Hennig, and M. Chergui, *J. Chim. Phys. Phys.-Chim. Biol.* **92**, 541 (1995); *J. Chem. Phys.* **101**, 7381 (1994); (b) *J. Phys. Chem.* (submitted); (c) J. Xu, P. Deitrich, N. Schwentner, S. Hennig, and M. Chergui, in *Femtochemistry: Ultrafast Chemical and Physical Processes in Molecular Systems*, edited by M. Chergui (World Scientific, Singapore, 1996), p. 305.
- ⁴⁸R. J. Sension and H. L. Strauss, *J. Chem. Phys.* **85**, 3791 (1986); **87**, 6221 (1987); R. J. Sension, T. Kobayashi, and H. L. Strauss, **87**, 6233 (1987); R. J. Sension and H. L. Strauss, **88**, 2289 (1988).
- ⁴⁹H. Kono and S. H. Lin, *J. Chem. Phys.* **84**, 1071 (1986).
- ⁵⁰M. Ben-Nun and R. D. Levine, *Chem. Phys.* **201**, 163 (1995); M. Ben-Nun, R. D. Levine, D. M. Jonas, and G. R. Fleming, *Chem. Phys. Lett.* **245**, 629 (1995).
- ⁵¹V. S. Batista and D. F. Coker, *J. Chem. Phys.* **105**, 4033 (1996).
- ⁵²P. Jungwirth and R. B. Gerber, *J. Chem. Phys.* **102**, 8855 (1995); P. Jungwirth, E. Fredj, and R. B. Gerber, **104**, 9332 (1996).
- ⁵³*Zero-Phonon Lines and Spectral Hole Burning in Spectroscopy and Photochemistry*, edited by O. Sild and K. Haller (Springer, Berlin 1986).
- ⁵⁴A. Cenian, S. Hennig, and H. Gabriel, *J. Chem. Phys.* **103**, 9276 (1995).
- ⁵⁵A. Borrmann and C. C. Martens, *J. Chem. Phys.* **102**, 1905 (1995).
- ⁵⁶G. van der Zwan and J. T. Hynes, *J. Phys. Chem.* **89**, 4181 (1985); E. A. Carter and J. T. Hynes, *J. Chem. Phys.* **94**, 5961 (1991).
- ⁵⁷M. Maroncelli, *J. Chem. Phys.* **94**, 2084 (1991); M. Maroncelli, V. P. Kumar, and A. Papazyan, *J. Phys. Chem.* **97**, 13 (1993).
- ⁵⁸L. Perera and M. L. Berkowitz, *J. Chem. Phys.* **96**, 3092 (1992); **97**, 5253 (1992).
- ⁵⁹E. Neira and A. Nitzan, *J. Chem. Phys.* **96**, 5433 (1992).
- ⁶⁰V. S. Filinov, *Nucl. Phys. B* **271**, 717 (1986).
- ⁶¹L. S. Shulman, *Techniques and Applications of Path Integration* (Wiley, New York, 1986).
- ⁶²V. P. Maslov and M. V. Fedoryuk, *Semiclassical Approximation in Quantum Mechanics* (Reidel, Boston, 1981).
- ⁶³E. Wigner, *Phys. Rev.* **40**, 749 (1932); M. Hillery, R. F. O'Connell, M. O. Scully, and E. P. Wigner, *Phys. Rep.* **106**, 121 (1984).
- ⁶⁴G. Herzberg, *Molecular Spectra and Molecular Structure: I. Spectra of Diatomic Molecules* (Van Nostrand, Princeton, 1950).
- ⁶⁵C. Kittel, *Introduction to Solid State Physics* (Wiley, New York, 1956).
- ⁶⁶P. Casavecchia, G. He, R. K. Sparks, and Y. T. Lee, *J. Chem. Phys.* **77**, 1878 (1982).
- ⁶⁷(a) M. D. Feit and J. A. Fleck, *J. Chem. Phys.* **78**, 301 (1983); (b) R. Kosloff, *J. Phys. Chem.* **92**, 2087 (1988).
- ⁶⁸A. G. Marshall and Francis R. Verdun, *Fourier Transforms in NMR, Optical, and Mass Spectrometry* (Elsevier, Amsterdam, 1990).
- ⁶⁹C. Cohen-Tannoudji, B. Diu, and F. Laloë, *Quantum Mechanics* (Wiley, New York, 1977), Vol. I, p. 620.
- ⁷⁰See for example the discussion in Ref. 26.
- ⁷¹M. P. Allen and D. J. Tildesley, *Computer Simulations of Liquids* (Clarendon, Oxford, 1987).
- ⁷²C. H. Becker, P. Casavecchia, Y. T. Lee, R. E. Olson, and W. A. Lester, Jr., *J. Chem. Phys.* **70**, 5477 (1979).
- ⁷³C. H. Becker, P. Casavecchia, Y. T. Lee, R. E. Olson, and W. A. Lester, *J. Chem. Phys.* **70**, 5477 (1979).
- ⁷⁴W. G. Lawrence and V. A. Apkarian, *J. Chem. Phys.* **101**, 1820 (1994).
- ⁷⁵H. A. Kramers and W. Heisenberg, *Z. Phys.* **31**, 681 (1925).
- ⁷⁶Y. J. Yan and S. Mukamel, *J. Chem. Phys.* **85**, 5908 (1986).
- ⁷⁷The term "diffraction bands" was used in the original work, E. U. Condon, *Phys. Rev.* **32**, 858 (1928).
- ⁷⁸The same phenomenon is also referred to as "interference bands," see for example: J. Tellinghuisen, *Phys. Rev. Lett.* **34**, 1137 (1975); *Adv. Chem. Phys.* **60**, 299 (1985); P. M. Hunt and M. S. Child, *Chem. Phys. Lett.* **58**, 202 (1978).
- ⁷⁹A. G. Redfield, *Adv. Mag. Reson.* **1**, 1 (1965).
- ⁸⁰A. J. Legget, S. Chakravarty, A. T. Dorsey, M. P. A. Fisher, A. Garg, and W. Zwerger, *Rev. Mod. Phys.* **59**, 1 (1987).
- ⁸¹See for example, R. B. Gerber, V. Buch, and M. A. Ratner, *J. Chem. Phys.* **77**, 3022 (1982); N. Makri and W. H. Miller, *ibid.* **87**, 5781 (1987); G. Stock, *ibid.* **103**, 2888 (1995).
- ⁸²(a) J. Wang, R. J. Boyd, and A. Laaksonen, *J. Chem. Phys.* **104**, 7261 (1996), and references therein. (b) For treatments of the dissociative A←X absorption of matrix isolated I₂, by the hybrid quantum/classical method, see L. Liu and H. Guo, *J. Chem. Phys.* **103**, 7851 (1995); **104**, 528 (1996).
- ⁸³See Ref. 11, and references therein.
- ⁸⁴J. Cao and G. A. Voth, *J. Chem. Phys.* **101**, 6184 (1994), and references therein.
- ⁸⁵B. B. Laird and J. L. Skinner, *J. Chem. Phys.* **94**, 4405 (1991), and references therein.
- ⁸⁶V. E. Bondybey and C. Fletcher, *J. Chem. Phys.* **64**, 3615 (1976).
- ⁸⁷V. A. Apkarian, in *Ultrafast Phenomena X* (Springer, Berlin, 1996); R. Zadayan, M. Sterling, and V. A. Apkarian (manuscript in preparation).